Systematic study of short- and long-range correlations in RE3TaO7 weberite-type compounds by neutron total scattering and X-ray diffraction

Igor Gussev, Eric O'Quinn, Matthew Tucker, Rodney Ewing, Cale Overstreet, Jörg Neuefeind, Michelle Everett, Qiang Zhang, David Sprouster, Daniel Olds, et al.

Systematic study of short- and long-range correlations in RE_3TaO_7 weberite-type compounds by neutron total scattering and X-ray diffraction

Igor M. Gussev [1,2], Eric C. O'Quinn [2], Matthew Tucker [3], Rodney C. Ewing [4], Cale Overstreet [2], Jörg Neuefeind [3], Michelle Everett [3], Qiang Zhang [3], David Sprouster [5], Daniel Olds [6], Gianguido Baldinozzi[1], Maik Lang [2].

1 Laboratoire Structures, Propriétés et Modélisation des Solides, CNRS, CentraleSupélec, Université Paris-Saclay, Gif-sur-Yvette, 91190, France

2 Department of Nuclear Engineering, University of Tennessee, Knoxville, TN, 37996, USA

3 Neutron Sciences Directorate, Oak Ridge National Laboratory, Oak Ridge, TN, 37830, USA

4 Department of Geological Sciences, Stanford University, Stanford, CA, 94305, USA

5 Department of Materials Science and Chemical Engineering, State University of New York, Stony Brook, NY, 11794, USA

6 National Synchrotron Light Source II, Brookhaven National Laboratory, Upton, NY, 11973, USA

Abstract

The atomic structures of the lanthanide tantalates, Ln_3TaO_7, series (Ln = Pr, Tb, Dy, Ho, Tm, Yb) were systematically investigated using total scattering techniques. High-energy X-ray and neutron diffraction analysis revealed that the long-range structures can be grouped into three distinct families: (*1*) ordered *Cmcm* (Ln = Pr), (*2*) ordered *Ccmm* (Ln = Tb, Dy, Ho), and (*3*) disordered, defect-fluorite *Fm-3m* (Ln = Ho, Tm, Yb). These findings help to clarify the symmetry discrepancy for the already reported long-range structures in literature. The short-range analysis of neutron total scattering data *via* pair distribution functions reveals a high degree of structural heterogeneity across length scales for all compounds, with distinct local atomic arrangements that are not fully captured by the average, long-range structure. The short-range structures at the level of coordination polyhedra are better captured by a set of alternative non-centrosymmetric structural models: (*1*) *C2cm*, (*2*) $C222_1$, and (*3*) *C2mm*. This establishes a short-range multiferroic character for weberite-type tantalates because ferroelectric interactions compete with magnetic correlations. These ferroelectric interactions are particularly pronounced for the disordered compounds Tm_3TaO_7 and Yb_3TaO_7. The structural differences among the three families are the result of changes in TaO_6 polyhedral tilt (transition between families 1 and 2) and dipolar interactions of off-centered Ta cations (transition between families 2 and 3).

Introduction

The chemical and structural flexibility of compounds derived from the mineral weberite (Na_2MgAlF_7, *Imma*) (1) displays a diverse array of physical properties, such high ionic conductivity, magnetic ordering, ferroelectricity, and photocatalytic activity (2–8). These properties make weberite-derived compounds of interest for water splitting photocatalysts (5,9), solid oxide fuel cell electrolytes (10), thermal barrier materials (11,12), and for applications exploiting their magnetic and dielectric properties (2,13–15). A specific subset of weberite-derived compounds, the $A^{III}{}_3B^{V}O_7$ *weberite-type* oxides (1), exhibit a greater variety of cation environments (allowing broader cation sizes and charge states) with respect to the weberite oxides ($A^{II}{}_2B^{V}{}_2O_7$), as well as to other topologically-related oxides (*e.g.*, $A_2{}^{III}B_2{}^{IV}O_7$ pyrochlore). For this reason, many different structural models have been proposed in the literature (15–17)for weberite-type oxides making an unambiguous classification of $A^{III}{}_3B^{V}O_7$ compounds into different structural families challenging.

The structures of A_3BO_7 weberite-type oxides (where A = lanthanide, B = Ta, Nb, Sb) (18),(19) are related to the fluorite structure and are generally best described by an orthorhombic supercell with unit-cell parameters $2a_F, \sqrt{2}a_F, \sqrt{2}a_F$. Initially, structures such as weberite, disordered fluorite, and disordered pyrochlore (18) were proposed for weberite-type compounds based on laboratory diffraction experiments (X-rays and/or electrons). Later, a comprehensive study was performed by Allpress *et al.*, who proposed, based on X-ray diffraction and selected-area electron diffraction (SAED) experiments (15–17,20), three distinct structure types for describing weberite-type oxides with different chemical composition. Allpress *et al.* proposed that the size of the A-site lanthanide cation influences their final symmetry, as trivalent lanthanides exhibit a monotonic contraction of ionic radius with increasing atomic number. Results from X-

ray diffraction experiments (in some cases revealed by SAED) (16),(21) were used to assign *Cmcm* (space group 63) to compounds with larger lanthanides (*e.g.*, La_3TaO_7, La_3NbO_7, La_3SbO_7, and Nd_3NbO_7), the *C222₁* (space group 20) to lanthanides with intermediate-sized ionic radius (*e.g.*, Gd_3TaO_7, Gd_3NbO_7, and Ho_3TaO_7), and the *Fm-3m* (space group 225) to compounds with smaller lanthanide cations (*e.g.*, Er_3NbO_7 and Er_3TaO_7). For the smaller lanthanide compounds, no supercell diffraction maxima were observed, and their diffraction patterns corresponded to a disordered, defect-fluorite structure with randomly distributed anion vacancies and random cation occupancy across the two available sites (16). Finally, weberite-type oxides at phase boundaries between structure types can exhibit different structures depending on the thermal history and temperature conditions during data collection (8). For example, according to Wakeshima *et al.*, compounds with intermediate sized cations, such as Ho_3TaO_7, display a *C222₁* symmetry after prolonged annealing at 1673 K or a *Fm-3m* symmetry after annealing at 1973 K (15). Similarly, Nd_3TaO_7 displays two polymorphs at room temperature, a mixture of *Cmcm* and *C222₁* phases, that transform into a single *C222₁* phase at higher temperature (15),(16) .

After those seminal studies, other research groups have investigated the structure of several weberite-type oxides mostly belonging to the initially assigned *C222₁* space group (intermediate-sized lanthanides, *e.g.*, Sm_3TaO_7 – Ho_3TaO_7 and Y_3TaO_7), though alternative structural models were sometimes proposed (17). The motivation for this reassessment was based on previously overlooked weak diffraction maxima, hardly detected in XRD patterns measured with laboratory diffractometer, but disagreeing with the selection rules of the *C222₁* symmetry. Space groups with mutually incompatible selection rules, such as *Cmcm* (or an alternative *Ccmm*, 63), *C222₁* (20), *Cmmm* (65), *Amm2* (38), *Cmm2* (35), and *C222* (21), were proposed for some of these compounds (15–17,20). The fact that so many different space groups have been proposed can be explained by

large uncertainties of refinements resulting from weak and overlapping peaks of powder diffraction data.

Looking in perspective to the set of proposed space groups, common trends emerge for ordered weberite-type tantalates, as these structures share similar structural motifs. The 6-coordinated B-site cations (Ta) form rigid TaO_6 octahedra, while A-site cations (Ln, Y) occupy two distinct polyhedra: AO_8 and AO_7 distorted cubes. In case of AO_7 polyhedra, one of the fluorite oxygen atoms is replaced by a vacancy. The TaO_6 octahedra share one corner with each other and form infinite chains projected along one of the shorter orthorhombic directions, typically the *c*-lattice parameter [001]. AO_8 distorted cubes share edges and form chains also parallel to [001]. These two chains form layers parallel to (100) with layers made of distorted AO_7 cubes between them (**Figure 1 b and c**). While the weberite-type structure is complex, it is constrained by the orthorhombic *c*-lattice parameter, which is a function of the size and tilt of the octahedra. This in turn imposes geometric constraints upon the other polyhedra, leading to distortions in most of the weberite-type compounds. All structural models proposed in literature for orthorhombic weberite-type compounds contain the same polyhedra arrangements with specific distortions: the main difference between them is the orientation of the tilt axis of the BO_6 octahedra. Indeed, *Cmcm* structures have a [010] tilt system, as shown in **Figure 1(*b*),** while *Ccmm* (or $C222_1$) structures have a [100] tilt system, as shown in **Figure 1(*c*)**. For the reader's convenience, we will refer to these structure types as ordered weberite-type families 1 and 2, respectively rather than by the actual space group definitions.

In this paper, we have used state-of-the-art spallation neutron and synchrotron X-ray scattering techniques to gain detailed insight into the structural complexity of weberite-type oxides that arises from proposed incompatible structural models and symmetries. Weberite-type

tantalates, covering a large range of lanthanide cation with different structures were synthesized and investigated across the long-range structure by means of combined neutron and X-ray diffraction experiments. The short-range structure was characterized *via* pair distribution analysis to describe the atomic arrangement and coordination polyhedra within the different long-range structures. This comprehensive analytical approach with high sensitivity to both the cation and anion positions provides a more unified description of the three structural families of weberite-type tantalates across different length scales.

Experimental methods

Sample synthesis

Polycrystalline powders of A_3TaO_7 (A = Pr, Tb, Dy, Ho, Tm, Yb) were synthesized using a solid-state reaction process. Powders of tantalum, praseodymium, terbium, dysprosium, holmium, thulium, and ytterbium oxides with a purity of 99.9998% were used as starting materials. The powders were preheated in air at 1000 K for 12 hours to remove any moisture and subsequently mixed, ground, and pressed into pellets. These pellets were heated in air at 1200 K for 48 hours, re-ground and pressed into pellets, and reheated in air at 1600-1673 K for 140 hours with several intermediate re-grinding steps. Ordered, orthorhombic weberite-type Ho_3TaO_7 was prepared by annealing at 1673 K, while the disordered, defect-fluorite type Ho_3TaO_7 was prepared by annealing at 1973 K. All sample compositions were chosen based on their advantageous neutron scattering properties such as: sufficient scattering lengths and low neutron absorption cross-section.

High-Energy synchrotron X-ray diffraction

High-energy synchrotron X-ray diffraction (SXRD) was performed on Pr_3TaO_7, Dy_3TaO_7, and Ho_3TaO_7 at the Pair Distribution Function beamline (28-ID-1) of the National Synchrotron Light Source-II (NSLS-II) at Brookhaven National Laboratory (BNL). Additionally, a previously characterized Y_3TaO_7 structure (22) was re-measured under identical conditions and served as a reference sample. All samples were placed in an airtight Kapton tube sample containers with 1 mm diameter and 0.6 μm wall thickness with plastic stoppers on both ends. These containers were mounted on a customized holder system, to allow for in-beam vertical movement to homogenize powder diffraction intensity and minimize potential texture effects. In addition, a LaB_6 calibration

standard and an identical empty sample container were mounted on the same holder to provide calibration data and to subtract the Kapton background intensity. The high-energy X-ray diffraction data were acquired with an exposition time of 1 minute with a photon energy of 74.47 KeV (λ of 0.1665 Å). The X-ray powder diffraction data were acquired as 2D diffractograms in a high-energy diffraction setting using the Perkin Elmer XRD 1621 detector.

High-resolution neutron diffraction

High-resolution neutron diffraction measurements were performed on Pr_3TaO_7 and Ho_3TaO_7 samples using the POWGEN (23) time-of-flight diffractometer at the beamline BL-11A at the Spallation Neutron Source (SNS), Oak Ridge National Laboratory (ORNL). The measurements were performed with 4 hours exposure time per sample at room temperature using the frame 2 setting of the diffractometer (λ of 0.97-2.033 Å with center wavelength of 1.5 Å). The samples were placed into 6 mm vanadium cans and filled with helium exchange gas before the measurement. The calibration standard, empty sample containers and vanadium rod were measured separately before the measurement to collect the data to be used in background subtraction and normalization. The POWGEN Automatic Changer (PAC) was used as the sample environment, which allowed measurements within a temperature region of 10-300 K. An additional low-temperature neutron diffraction measurement was performed at 100 K on Ho_3TaO_7, using otherwise similar measurement conditions and data processing procedures.

Neutron total scattering

Neutron total scattering characterization was performed on Pr_3TaO_7, Tb_3TaO_7, two polymorphs of Ho_3TaO_7, Tm_3TaO_7, and Yb_3TaO_7, using the time-of-flight Nanoscale-Ordered

Materials Diffractometer (NOMAD) (24) at the beamline BL-1B at the SNS. All samples were loaded into 2 mm quartz capillaries with a wall thickness of 0.01 mm. The measurements were performed at room temperature with an exposure time of 64 minutes per sample. The six NOMAD detector banks were calibrated using scattering from a diamond powder and silicon sample. The silicon standard was used to obtain the instrument parameter file for the Rietveld refinements. The scattering intensity from an empty sample position as well as from an empty 2 mm quartz capillary were measured as background signals and automatically subtracted from the scattering intensity of the polycrystalline powder samples. The resulting scattering intensity of each sample was normalized to the scattering intensity of a solid vanadium rod to account for the spallation neutron spectrum. A Fourier transform was applied to the structure functions, S(*Q*), to obtain the pair distribution function,

$$\mathrm{G\,(r)} \;=\; A * \mathrm{Q}_{max} \int_{Qmin}^{Qmax} \mathrm{Q(S(Q)-1)Sin(Qr)dQ} \qquad \text{(Eq. 1)}$$

where the maximum momentum transfer (Q_{max}) was 31.4 Å^{-1} and *A* is an arbitrary scale parameter determined during small-box modeling. The momentum transfer is defined as: $Q = 4\pi\sin\theta/\lambda$, where λ and θ are the neutron wavelength and scattering angle, respectively. Additional low-temperature neutron total scattering measurements were performed for Pr_3TaO_7, Ho_3TaO_7, and Yb_3TaO_7 at 100 K using an otherwise identical instrument setup and data processing scheme.

Data analysis

The long-range structure was analyzed using Rietveld refinement performed in the GSAS (25) and GSAS-II (26) packages. The highest *Q*-resolution backscattering detector banks (3, 4, and 5) with different *Q*-space coverage and resolution were refined simultaneously for the NOMAD diffraction data, resulting in a single cumulative reliability factor parameter (R-factor), referred to as *wRp* in GSAS-I, software or *Rw* in this study to avoid confusion. The POWGEN and SXRD diffraction data were refined using a single detector bank. During refinement of the POWGEN data, the diffraction patterns were divided into two *d*-space regions to minimize the effect of varying instrumental resolution across the large detector coverage in *d*-space. Therefore, the reliability factor is reported as two separate values (Rw_1 and Rw_2) for POWGEN diffraction data and as single value (*Rw*) for SXRD data. For all symmetries used, the following sets of parameters were refined: 6 Chebyshev background parameters, scale factor, respective unit cell dimensions ($a \neq b \neq c$ for orthorhombic cells, $a = b = c$ for cubic cells), respective allowed positional parameters and harmonic U*ij* for POWGEN diffraction and isotropic U_{iso} for NOMAD and SXRD diffraction for individual atomic sites.

Small-box refinements of neutron pair distribution functions (PDFs), representing the short-range structure, were performed using the PDFgui software (27). Similar to the long-range refinement, scale factor, PDFgui specific *delta2* parameter (to account for the correlated displacements of the distances between nearest neighbors), allowed unit cell parameters ($a \neq b \neq c$, $\beta \neq 90°$ for monoclinic cells, $a \neq b \neq c$ for orthorhombic cells, and $a = b = c$ for cubic cells), and positional parameters were refined. Depending on the refinement type (discussed later in more detail), both isotropic (U_{iso}) and harmonic (U_{ij}) atomic displacement parameters (ADP) were used for each applicable atomic site. The VESTA (28) software was used to visualize and produce all

3-D structural images for visualization and interpretation, as well as to extract necessary polyhedra information. So-called 'boxcar' refinements were performed using PDFgui software with *r*-series macros, using the initial parameters of each refinement from previous fits. The initial fit range was set as 1.5-12 Å (10.5 Å fit window), with subsequent fits performed by increasing the minimum *r*-value (r_{min}) in 1 Å increments while keeping the same fit window size (*i.e.*, 2.5– 13 Å, 3.5-14 Å, etc.).

In both Rietveld and small box refinement, the cumulative *R*-factor (reliability factor, *Rw*) was defined as following:

$$R_w = \sqrt{\frac{\sum_{i=1}^{N} w(r_i)[G_{obs}(r_i) - G_{calc}(r_i)]^2}{\sum_{i=1}^{N} w(r_i) G_{obs}^2(r_i)}} \qquad \text{(Eq. 2)}$$

Where G_{obs} and G_{calc} are observed and modelled intensities at point r_i, and $w(r_i)$ is weighting factor, defined by the uncertainty in the data file.

In addition to the *R*-factor analysis of the PDF data, the *S*-factor analysis technique was adopted in this study. This was based on the diffraction data refinement approach and used here to estimate the limits of the local correlations and calculate the *correlated reliability factor* (*Gs*) for PDF data. Adopting equation 6 from (29), *Gs* is defined accordingly for the real space $G(r)$ data:

$$G_s = \sum_{j \in uncorrelated\ region} w_j \left(G_{obs}(r_j) - G_{calc}(r_j)\right)^2$$

$$+ \sum_m \left(\sum_{k \in correlated\ region} w_k^{1/2} \left(G_{obs}(r_k) - G_{calc}(r_k)\right) \right)^2 \qquad \text{(Eq. 3)}$$

Where the first summation is the usual one; whereas the second summation, over *k*, is only defined on sets of neighboring points within each correlation region m, and it is the simple square of the sum of the *G(r)* differences, which are further summed across all correlated regions. The

parameters G_{obs} and G_{calc} are the observed and calculated intensities at each point of *G(r)*, respectively. Two neighboring points are deemed correlated when the product of their differences across two points have the same sign and the modulus exceeds a specific threshold value, that is a chosen function of the statistical weights w_j:

$$|(G_{obs}(r_i) - G_{calc}(r_i)) * (G_{obs}(r_{i-1}) - G_{calc}(r_{i-1}))| > \ threshold$$

When the points are deemed uncorrelated, the *Gs* calculations fall back to the unnormalized *Rw* expression (Eq. 2); however, the length of the correlated regions dramatically affects the *Gs* value. A set of threshold values based on the confidence interval of the *G(r)* values was then used to identify the regions where the error is correlated. The advantage of using *Gs* instead of *Rw* for the PDF analysis is that the *Rw* factor is biased by the assumption of uncorrelated errors, whereas *Gs* accounts for systematic correlations within the difference curve.

The maximum *r*-value (r_{max}) used for the refinements is relatively large, typically bigger than the largest dimension of the unit-cell used for the different structural models (r_{max} ~ 12Å). Therefore, the *Rw* value is less sensitive to the fit quality in the low-*r* region (< 5Å), most important to the distortions of the coordination polyhedra, because it includes the contributions at high-*r* from the higher order atomic correlations (*e.g.*, second-, third-, … nearest neighbors). In addition, the PDF data across different sample compositions is affected by a scattering-length 'efficiency' effect due to the presence of different lanthanide ions. For example, the scattering length of Yb is 12.4 fm, which is approximately twice than the scattering length of O (5.80 fm) or Ta (6.91 fm). Therefore, the signal from Yb-Yb pair correlations dominates the refinement (as these peaks are typically much more intense than the corresponding O-O pair correlations); this effect in turn affects the difference curve and the calculation of the *Rw* value. This bias can be somewhat adjusted by limiting the *r*-range of the PDF refinement to the region sensitive to the coordination

polyhedra and the nearest neighbor distances (r_{max} ~ 4.2 Å). Over this fit range, only cation-oxygen and oxygen-oxygen correlations are typically present, which reduces the relative impact of the scattering lengths of the different lanthanides. As a result, the difference curves between fit and experimental data are more comparable across the different sample compositions.

Analytical derivation of the weberite-type structure

Before new experimental data are presented, general aspects of the weberite-type structures are assessed, which will help to contextualize and better interpret the results presented in this study. In weberite-type tantalate oxides, the charge difference between the two cations (Ln^{+3} and Ta^{+5}) can favor long-range order, with both cations and anions at specific crystallographic sites. This 0defines a specific bonding environment resulting in a repeating configuration of four different coordination polyhedra: (*i*) an octahedron, formed by the pentavalent Ta cation, (*ii*) and (*iii*) two sevenfold-coordinated polyhedra, occupied by the rare-earth or lanthanide cations, typically in form of a mono-capped octahedral configuration, and (*iv*) an eightfold-coordinated distorted cube, occupied by the lanthanide cation. Moving across the Ln^{3+} series from Pr to Yb, the size of the lanthanide ions contract, which influences the tilt and deformation modes of the stiffer Ta-octahedron, leading to structural changes in the other three more flexible Ln-polyhedra. For the smallest lanthanide cations, these changes lead eventually to a loss of the long-range order, folding the orthorhombic weberite-type structure into a disordered, defect-fluorite structure. In this disordered structure, the two cations randomly occupy a shared cation site; whereas, the oxygen vacancy is statistically distributed onto the anion sites. However, recent results on weberite-type oxides with the defect-fluorite structure (30) and structurally-related pyrochlore oxides suggest that short-range ordered correlations persist within such disordered compounds that are distinct

from the average long-range structure (22,31–34). In contrast, ordered weberite-type Ln_3TaO_7 oxides exhibit small distortions with respect to the parent fluorite structure, leading to an orthorhombic lattice with pseudo-tetragonal characteristics. To simplify the presentation of the results, a unique reference lattice is defined, assuming $a_W = 2a_F$ and $b_W \approx c_W \approx a_F\sqrt{2}$, with "*W*" and "*F*" subscripts referring to weberite and fluorite lattices, respectively. This orientation convention is not always adopted in previous studies, but it aids in discussing and comparing the structural changes across all weberite-type oxides. In this reference frame, a set of two Ta octahedra form corner-sharing chains along the *c*-axis. As a result, half of the distorted octahedra tilt clockwise around either the a_W or the b_W axes, while the other half in the next atomic layer tilts counterclockwise. The extent of the octahedron distortion and the actual tilt axis determine the overall length of the c_W-axis parameter and the final symmetry of the space group.

As described before, three main space groups have been defined previously to describe the structures of Ln_3TaO_7 weberite-type tantalates: *Cmcm*, *Ccmm* (*or* $C222_1$), and *Fm-3m* (**Figure 1b, c**). The use of these different structural models can be rationalized based on a prototype 'parent' structure, for which tilts and distortions are removed. This prototype (P) structure (**Figure 1a**), which is described in detail in the supplementary information (**Supplementary Table 1**), has a *Cmmm* (65) symmetry with a *c*-lattice parameter that is halved as compared with that of the C-centered weberite-type structures ($a_P = a_W$, $b_P = b_W$, and $c_P = ½\ c_W$).

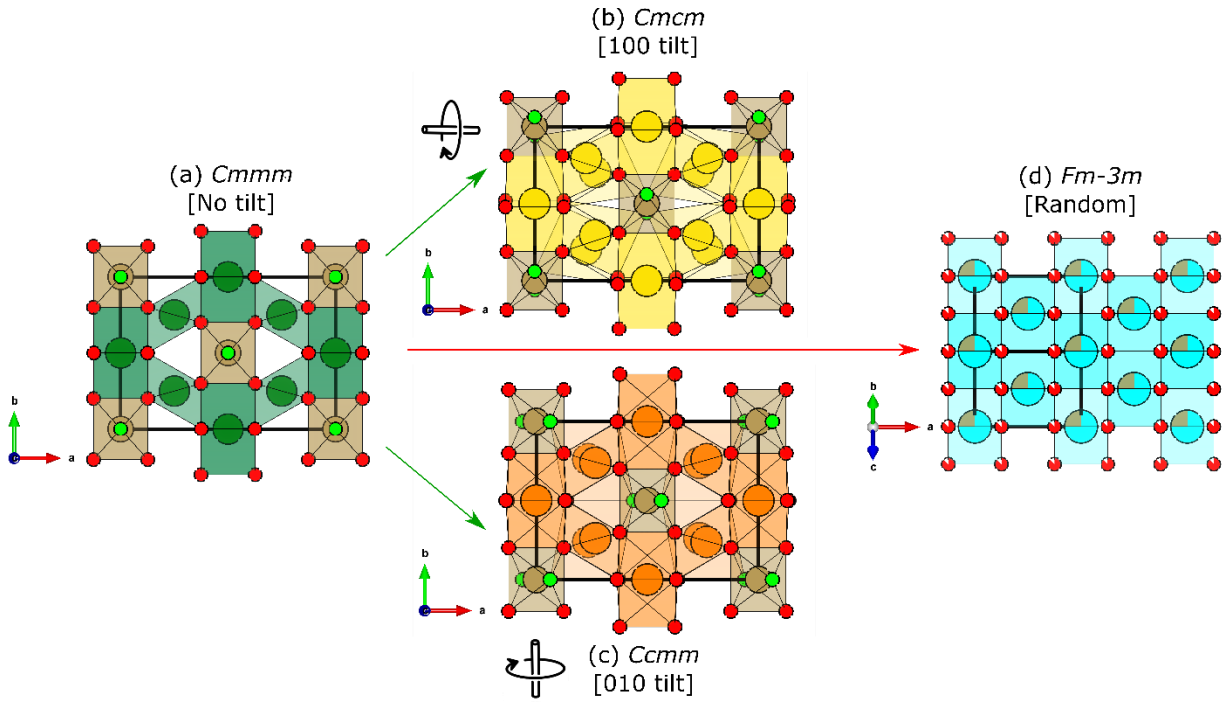

Figure 1: Relations among the three structural families of A_3TaO_7 weberite-type oxides (*b*,*c*,*d*). The structures are shown with the relation to the single c-layer parent prototype structure. Thick solid black lines represent the respective unit cells. (*a*) *Cmmm* prototype model with A-site cations shown as green spheres, (*b*) *Cmcm* structural model with large radii A-site cations shown as yellow spheres, (*c*) *Ccmm* structural model with medium radii A-site cations shown as orange spheres and (*d*) *Fm-3m* structural model with small radii A-site cations shown as cyan spheres. Oxygen anions and Ta cations are shown in all four structures as red and brown spheres, respectively. Oxygen anions highlighted as smaller lime green spheres and displaced according to different tilt systems. The tilt systems of the (*a*) single layer *Cmmm* prototype structure produce either the bilayer structure (*b*) *Cmcm* with [100] tilt, or the (*c*) *Ccmm* with [010] tilt, as represented by black loops around the rotation axes. The white sectors within red spheres in (*d*) denote the partial occupancy of oxygen sites in the *Fm-3m* model, and mixed brown/cyan spheres represents a randomization of cations across cation sites. All coordination polyhedra are shown according to the color of their respective cations. Structures are projected along their conventional directions: (*a*,*b*,*c*) along $[001]_W$ and (*d*) $[011]_F$ with W and F subscripts denoting the weberite-type and defect-fluorite lattices, respectively.

The most common structural models proposed in the literature for niobates and tantalates weberite-type compounds can be derived using mechanical instabilities of the irreducible representations at the Y, T, and Z points of the centered orthorhombic Brillouin zone of the prototype weberite structure. All structures of the Ta-based compounds reported in literature can be obtained systematically by considering Z-point irreducible representations. The most symmetric structural models belonging to these 8 irreducible representations are described by four centrosymmetric space groups, each one with two distinct origins: Z_1^+, Z_2^- lead to *Cmmm* (65), Z_2^+, Z_1^- to *Cccm* (66), Z_3^+, Z_4^- to *Cmcm* (63), and Z_4^+, Z_3^- to *Ccmm* (63). Eventually, these space group symmetries can be further reduced if specific peaks in the diffraction patterns provide the required evidence. For instance, suppression of the inversion center in either *Ccmm* or *Cmcm* yields the $C222_1$ symmetry. The different space groups are characterized by distinct supercell peaks, which can be compared with high quality diffraction data to identify the most appropriate model for any particular compound.

Results

Long-range structural analysis

High-energy synchrotron X-ray (SXRD) diffraction data were collected for the ordered, orthorhombic Pr_3TaO_7, Dy_3TaO_7 and Ho_3TaO_7 samples and refined using structural models previously reported in literature (15–17) (*Cmcm* for Pr_3TaO_7; *Ccmm* or Dy_3TaO_7 and Ho_3TaO_7, (**Figure 2a**). All refinements provided reasonable fits as demonstrated by the difference curves and acceptable reliability factor (*Rw*) parameters. Only the refinement of the Pr_3TaO_7 diffraction pattern resulted in a slightly larger *Rw*, which can be explained by the presence of a minor impurity phase (less than 3% of $PrTaO_4$). No impurities were detected in the XRD patterns of Ho_3TaO_7 and Dy_3TaO_7.

Inspection of the low-*Q*/high *d*-spacing part of the diffraction patterns is critical for establishing the correct space group for the different weberite-type compounds. This region is very sensitive to site occupancy and atomic order, which produces separate peaks in the synchrotron X-ray and neutron diffraction patterns. Of particular importance is the presence, or absence, of *0kl* and *h0l* peaks: (*e0o*) like (201), (401), or (403) are allowed by *Ccmm* and forbidden for *Cmcm*; *vice versa*, (*0eo*) like (021), (041), (043) are allowed by *Cmcm* and forbidden for *Ccmm*. If the peaks of both sets are observed in the diffraction patterns, the inversion center is suppressed. This was experimentally demonstrated for the structure of the rare-earth compound Y_3TaO_7 (22), described by the $C222_1$ space group. While not being part of this study on lanthanide tantalates compounds, we have re-measured this sample (22) under identical high-energy SXRD conditions as reference data set to compare with the ordered weberite-type lanthanide compounds (**Figure 2b**).

Inspection of the low-*Q* region (**Figure 2b**) clearly shows that Pr_3TaO_7 exhibits a (021) diffraction maximum at ~1.85 $Å^{-1}$, while the (201) peak is absent. This agrees with the crystallographic rules of the *Cmcm* space group, which confirms that this structural model reported in literature is indeed the most symmetrical one for Pr_3TaO_7 and potentially for all the other members of structural family 1. Rietveld refinement with the *Cmcm* space group yields excellent agreement to the XRD data for Pr_3TaO_7 (*Rw* = 3.359%). The extinction rules are reversed for *Ccmm* and the low-*Q* diffraction regions of Ho_3TaO_7 and Dy_3TaO_7 of structural family 2 (**Figure 2b**); (201) peaks are observed at ~1.48 $Å^{-1}$, whereas (021) peaks are not observed at ~1.83 $Å^{-1}$. This agrees with the proposed *Ccmm* space group by Fu *et al.* for Sm_3TaO_7 (17), a compound of the same structural family. Refinement of the measured SXRD patterns of Ho_3TaO_7 and Dy_3TaO_7 with this *Ccmm* space group provides excellent agreement with very low *Rw* of 2.409% and 2.691%, respectively, confirming the choice of this highly symmetrical space group. The centrosymmetric nature of this space group is further corroborated by the reported absence of any second harmonic generation signal at room temperature, as described by Astafyev *et al.* (35) for Ln_3TaO_7 (Ln = Sm-Gd). Therefore, it is reasonable to expect that the *Ccmm* space group is the common representation for all structural family 2 compounds. On the other hand, the $C222_1$ symmetry is confirmed by the existence of (201) and (021) peaks in Y_3TaO_7 (**Figure 2b**), and this compound can no longer be considered as the room temperature structural model for the long-range structures of family 2 weberite-type tantalates.

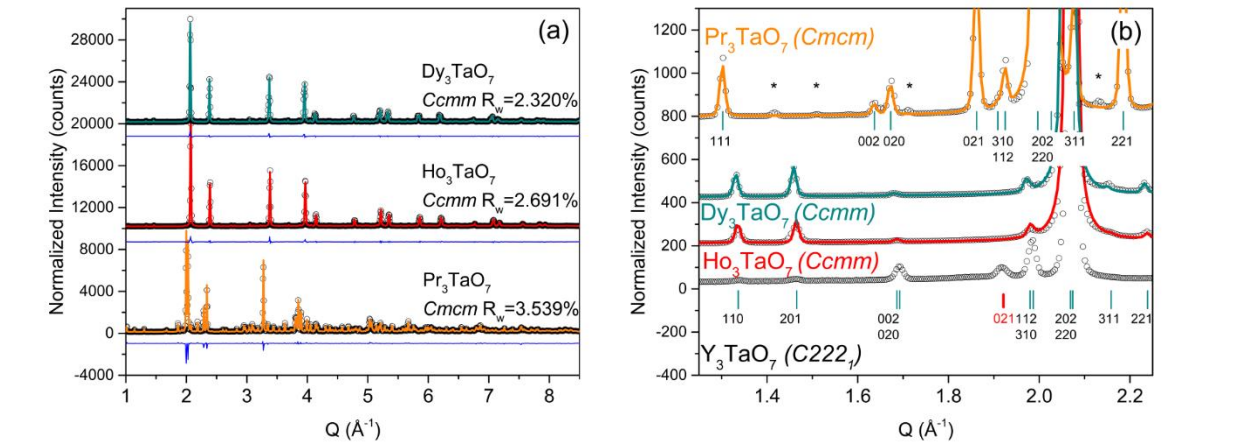

Figure 2: (a) Stacked high-energy synchrotron X-ray diffraction patterns for A_3TaO_7 (A = Pr, Dy, Ho) as measured (black circles) and modeled (orange, cyan and red curves). Blue curves represent the difference between measurement and calculated model (space groups *Cmcm* and *Ccmm*). The reliability factor (*Rw*) is reported for every sample. Diffraction patterns are offset by values of 10'000 and 20'000 respectively. (b) Expanded view of the low-Q range of (a) using the same color labeling, along with diffraction data of Y_3TaO_7 (black circles), which serves as reference measurement. Cyan ticks represent diffraction conditions allowed in (top) *Cmcm* and (bottom) *Ccmm* space groups. Asterisks (*) mark the $PrTaO_4$ impurity phase reflections for Pr_3TaO_7. The red tick mark at ~1.93 $Å^{-1}$ indicates the location of the (021) diffraction peak, which serves as space group distinction between $C222_1$ and *Ccmm* (and it is only allowed for $C222_1$). Diffraction patterns are offset by values of 200, 400 and 800 respectively. Enlarged version of this figure is available in the supplementary section.

Rietveld refinement of the high-resolution time-of-flight neutron diffraction patterns (POWGEN) with high sensitivity to the oxygen positions yielded a good agreement with the *Cmcm* model (Rw_1 = 2.501% and Rw_2 = 4.769%) for Pr_3TaO_7 **(Supplementary Figure 1**) and the *Ccmm* model (Rw_1 = 4.940% and Rw_2 = 4.770%) for ordered Ho_3TaO_7 (**Supplementary Figure 2**). The amount of $PrTaO_4$ impurity phase in Pr_3TaO_7 was 1.7%, and neutron characterization did not reveal any impurity phases in Ho_3TaO_7. In agreement with the SXRD results, the time-of-flight neutron diffraction results also show strong evidence of the (021) peak for Pr_3TaO_7 with no apparent signal of the (201) peak; whereas, Ho_3TaO_7 shows a pronounced (201) peak. The absence of the (021)

peak (expected at ~1.92 Å in *Q*-space or ~3.3 Å in *d*-space) confirms the centrosymmetric *Ccmm* model for Ho_3TaO_7 (**Supplementary Figure 3**). The diffraction pattern of Ho_3TaO_7 measured at 100 K with reduced effect of thermal vibrations show the same structural behavior and supports this conclusion (**Supplementary Figure 4**).

Neutron diffraction patterns of A_3TaO_7 (A=Pr, Tb, Ho, Tm, and Yb) collected at NOMAD revealed three distinct structures across the lanthanide series (**Figure 3**). Rietveld refinement confirms that these patterns belong to the three distinct structural families of weberite-type tantalates. The NOMAD diffraction patterns (**Figure 3**) are in good agreement with SXRD and POWGEN data obtained for the two ordered families. Family 1 is described by the orthorhombic *Cmcm* model (Pr_3TaO_7, *Rw* = 5.43%) and family 2 by the orthorhombic *Ccmm* model (Tb_3TaO_7 and Ho_3TaO_7 synthesized at 1673 K with *Rw* = 7.39% and 7.99%, respectively). As already reported in the literature (15,30), structural family 3 of disordered weberite-type tantalates is described by the defect-fluorite (*Fm-3m*) space group: disordered Ho_3TaO_7 synthesized at 1973 K, Tm_3TaO_7, and Yb_3TaO_7 , with *Rw* = 8.40%, 9.85% and 6.47%, respectively. The Pr_3TaO_7 refinement is the best in terms of cumulative *Rw* value among all samples, despite the minor impurity phase. The complete structural information obtained from Rietveld refinement of NOMAD data are summarized in **Supplementary Table 2**. In the disordered, defect-fluorite compounds, the orthorhombic superstructure peaks, characteristic of the weberite-type ordering, are only detectable as a weak and broad diffuse scattering signal, which carries information about specific short-range atomic correlations. These were analyzed in real space using pair distribution functions (PDFs) to obtain valuable insight into the atomic-scale structure of the different weberite-type oxides.

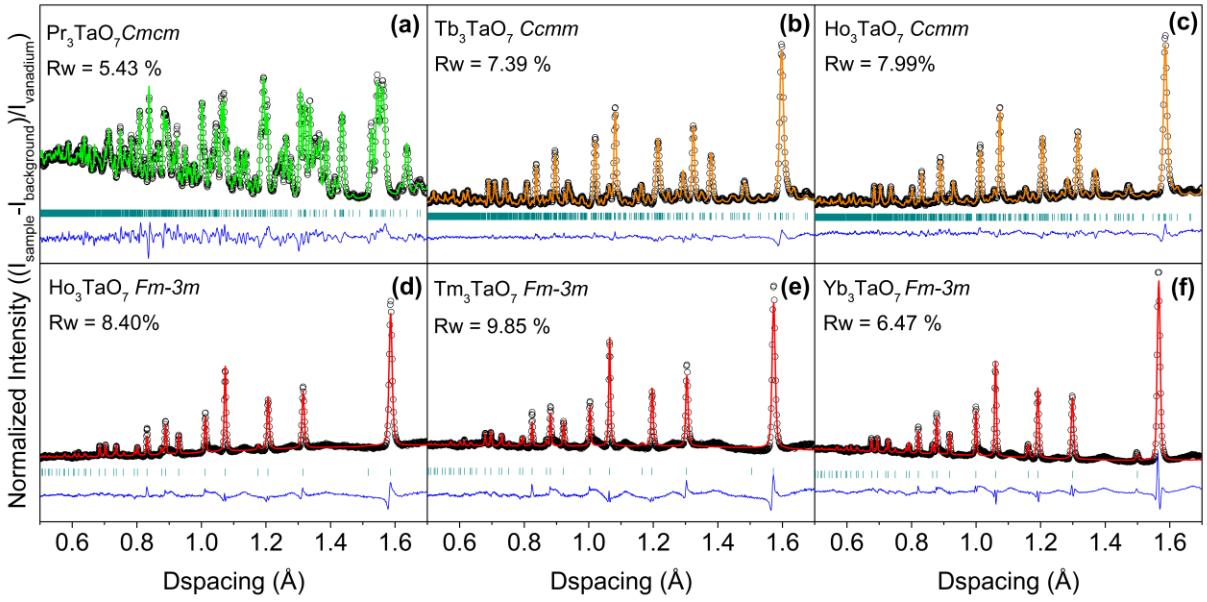

Figure 3: Neutron diffraction patterns of A_3TaO_7 (A=Pr, Tb, Ho, Tm, and Yb) measured at NOMAD's detector bank 4. The experimental data (shown as black circles) were refined using small-box modeling based on the following space groups: (**a**) *Cmcm* (green curve), (**b,c**) *Ccmm* (amber curve) and (**d,e,f**) *Fm-3m* (red curve). The blue curves are the difference between experimental data and calculated models. *Rw* values are reported for each refinement.

Short-range structural analysis

Analysis based on long-range derived structural models

High-resolution PDF data of all samples are shown in **Figure 4** over a *r*-range between about 2 Å and 11 Å. The peak positions are characteristic of specific atomic-pair correlations (sometimes leading to several unresolved contributions within one peak), the area under the peak depends on the coordination number, and the width is related to the spread of the interatomic distances that increases with the displacive disorder in the system. The PDFs across the sample series show variations in peak intensities and widths and, as a first step, the long-range structural models from diffraction data (**Figure 3**) were used for small-box modeling: *Cmcm* for weberite-type compounds with large lanthanides, *Ccmm* for the medium-sized lanthanides, and *Fm-3m* for

small lanthanides (**Figure 4**). All ordered orthorhombic models (either *Cmcm* or *Ccmm*) provide a reasonably good agreement with the experimental data (Pr_3TaO_7, Tb_3TaO_7, and long-range ordered Ho_3TaO_7, with *Rw* values typically less than 10%). However, refinement of long-range disordered Ho_3TaO_7, Tm_3TaO_7, and Yb_3TaO_7 with the *Fm-3m* defect-fluorite model resulted in an extremely poor fit quality (*Rw* values well above 20%) (**Figure 4**), which motivates further detailed analysis of the short-range structure, as discussed later in this section. The complete structural information obtained from PDF refinement of NOMAD data are summarized in **Supplementary Table 3**.

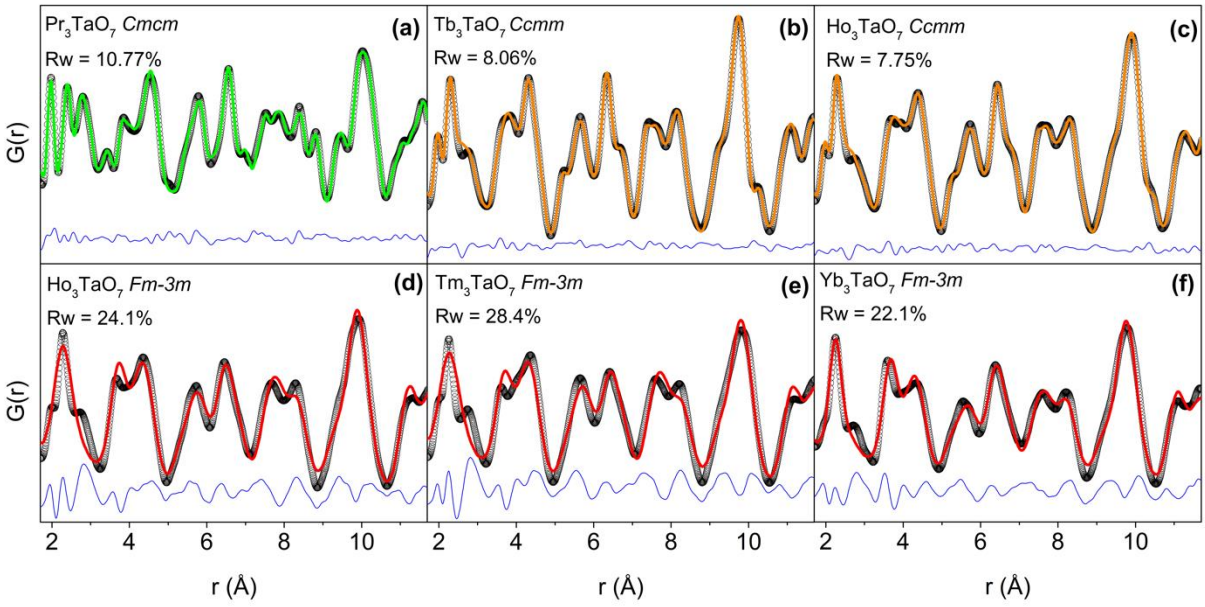

Figure 4: Neutron pair distribution functions (PDFs) of Ln_3TaO_7 (Ln=Pr, Tb, Ho, Tm, and Yb). Data (black circles) obtained at room temperature and modelled with long-range derived structural models (green, amber, and red curves for each family) using (**a**) *Cmcm*, (**b, c**) *Ccmm* and (**d, e, f**) *Fm-3m* space groups, respectively. The blue curves are the difference between the experimental data and the small-box refinement calculated models. *Rw* values are reported for each refinement.

Small-box analysis of weberite-type compositions with larger and medium sized lanthanides (ordered, orthorhombic structural families)

The previously reported *Cmcm* and *Ccmm* models, which described well the corresponding long-range structures of the ordered weberite-type samples, also provide a reasonably good agreement for the short-range data as expressed by the reasonably low *Rw* values. There was no strong dependence of the *Rw* values on the spatial range considered for these small-box refinements. However, there are certain PDF sections, particularly at ~2.9 Å, sensitive to O-O correlations in Tb_3TaO_7 and Ho_3TaO_7 (**Figure 5**, asterisks markers), that evidence systematic discrepancies between experiment and model. A similar behavior has been previously reported for weberite-type Y_3TaO_7, and changes in these O-O correlations were instrumental to the assignment of *C222₁* symmetry (22). On the other hand, there is no obvious localized systematic discrepancy between data and refinement for Pr_3TaO_7 (**Figure 5a**), but the *Rw* value is still somewhat higher than expected.

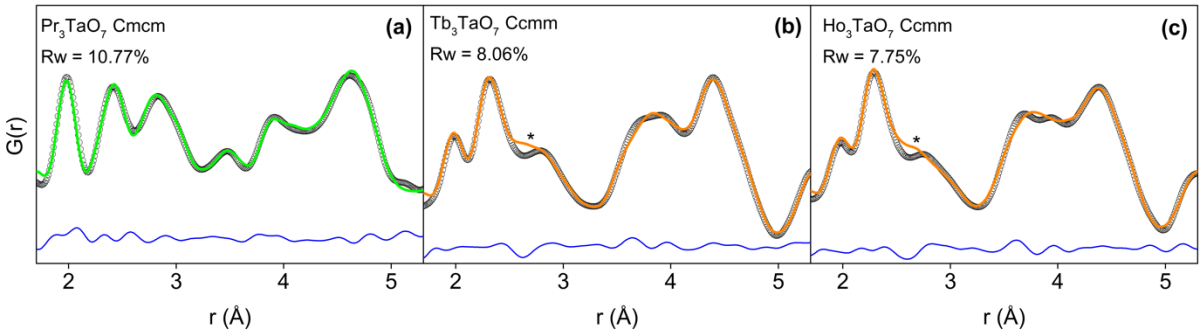

Figure 5: Enlarged view of the neutron PDFs of Fig. 5 covering the very local *r*-range (1.7-5.3 Å) where 1st and 2nd nearest neighbor correlations are observed in ordered weberite-type A_3TaO_7 (A=Pr, Tb, Ho) with (**a**) *Cmcm* and (**b, c**) *Ccmm* space group models, respectively. Black circles represent the experimental data and red lines are the refined models. The blue lines are the difference curves between data and the small-box refinements. *Rw* values are reported. Asterisk symbols (*) highlight the O-O correlation misfit of the *Ccmm* model at ~2.8 Å for Tb_3TaO_7 and Ho_3TaO_7.

To improve the small-box PDF refinement, a set of alternative symmetries were employed to improve the description of the displacive distortions affecting the O-O pair correlations. The approach was to systematically explore the subgroup structures deduced from the Brillouin zone center (Γ) irreducible representations of the respective *Cmcm* and *Ccmm* space groups corresponding to the long-range structures of weberite families 1 and 2, respectively. Seven additional structural models were derived for each space group. For the *Cmcm* model (Pr_3TaO_7, [100] tilt), the order parameter of the 8 irreducible representations (Γ) lead to the following space groups: *Cmcm* (63, (a, b, c), Γ_1^+), *P2₁/m* (11, unique axis c, Γ_2^+), *C2/m* (12, unique axis a, Γ_3^+) and *C2/c* (15, unique axis b, Γ_4^+), which are centrosymmetric, and the four non-centrosymmetric *C222₁* (20, (a, b, c), Γ_1^-), *Cmc2₁* (36, (a,b,c), Γ_2^-), *C2cm* (40, (-c, b, a), Γ_3^-), *Cm2m* (38, (b, c, a), Γ_4^-). For the *Ccmm* model (ordered Ho_3TaO_7, [010] tilt), the tested Γ-point space groups were: *Ccmm* (63, (b, a, -c), Γ_1^+), *P2₁/m* (11, unique axis b, Γ_2^+), *C2/m* (12, unique axis b, Γ_3^+) and *C2/c* (15, unique axis a, Γ_4^+) and the non-centrosymmetric counterparts *C222₁* (20, (b, a,-c), Γ_1^-), *Ccm2₁* (36, (b, a, -c), Γ_2^-), *Cc2m* (40, (b, c, a), Γ_3^-), *C2mm* (38, (-c, b, a), Γ_4^-). Initially, to provide the best model selectivity, the structural analyses were performed on Pr_3TaO_7 and ordered Ho_3TaO_7 measured at 100 K. Indeed, the low-temperature measurement greatly reduced the effect of thermal smearing and improved the positional parameter analysis for each compound representative of families 1 and 2 tilt systems. The quality of the fit for each model was evaluated by two criteria: *(i)* the conventional *Rw* value (*Eq. 2*) and *(ii)* the correlated *Gs*-value (*Eq. 3*), which 'penalizes' correlated errors of the difference curve, apart from purely stochastic deviations. The most accurate model is the one with the lowest *Rw* value and with the least correlated difference curve, particularly within the low-*r* PDF section sensitive to 1st and 2nd nearest neighbor correlations.

The results of this detailed PDF analysis with refinements based on these eight models are shown in **Figure 6** for Pr_3TaO_7 measured at 100 K. Qualitative inspection shows that most models describe the local structure of Pr_3TaO_7 quite well (**Figure 6a**), though some space group choices lead to unstable refinements and to an increased *Rw*. These models were rejected as unsuitable. *Rw* values reveal that non-centrosymmetric models ($\Gamma_{1\text{-}4}^-$) generally produce slightly better fits to the neutron PDF data as compared with centrosymmetric models ($\Gamma_{1\text{-}4}^+$), including the long-range *Cmcm* model, in particular. This reliability factor analysis favors in the *r*-range of 1.5 – 12 Å especially the *Cmc2₁* (Γ_2-), *C2cm* (Γ_3-), *Cm2m* (Γ_4-), *C2/c* (Γ_4+), and marginally *C222₁* (Γ_1-) models with *Rw* values close to 8%.

The *Gs*-factor analysis also demonstrates that non-centrosymmetric models are preferable as they generally have smaller *Gs*-values, indicative of reduced systematic errors. Considering both *Rw* and *Gs* criteria, this reduces the initial eight possible choices for the [100] tilt system to the models Γ_3^- (*C2cm*) and Γ_4^- (*Cm2m*). Providing similar agreement, both models were judged based on their number of refined parameters, which were 49 and 54, respectively. Thus, Γ_3^- (*C2cm*) is the preferred description of the coordination polyhedra environment and the best fit to the short-range structure of Pr_3TaO_7. This is supported by the evolution of the difference curve (**Figure 6b**), which exhibits only uncorrelated intensity fluctuations, specifically in the *r*-range significant for the critical O-O correlations (2.5 – 3 Å, shaded region in **Figure 6b**).

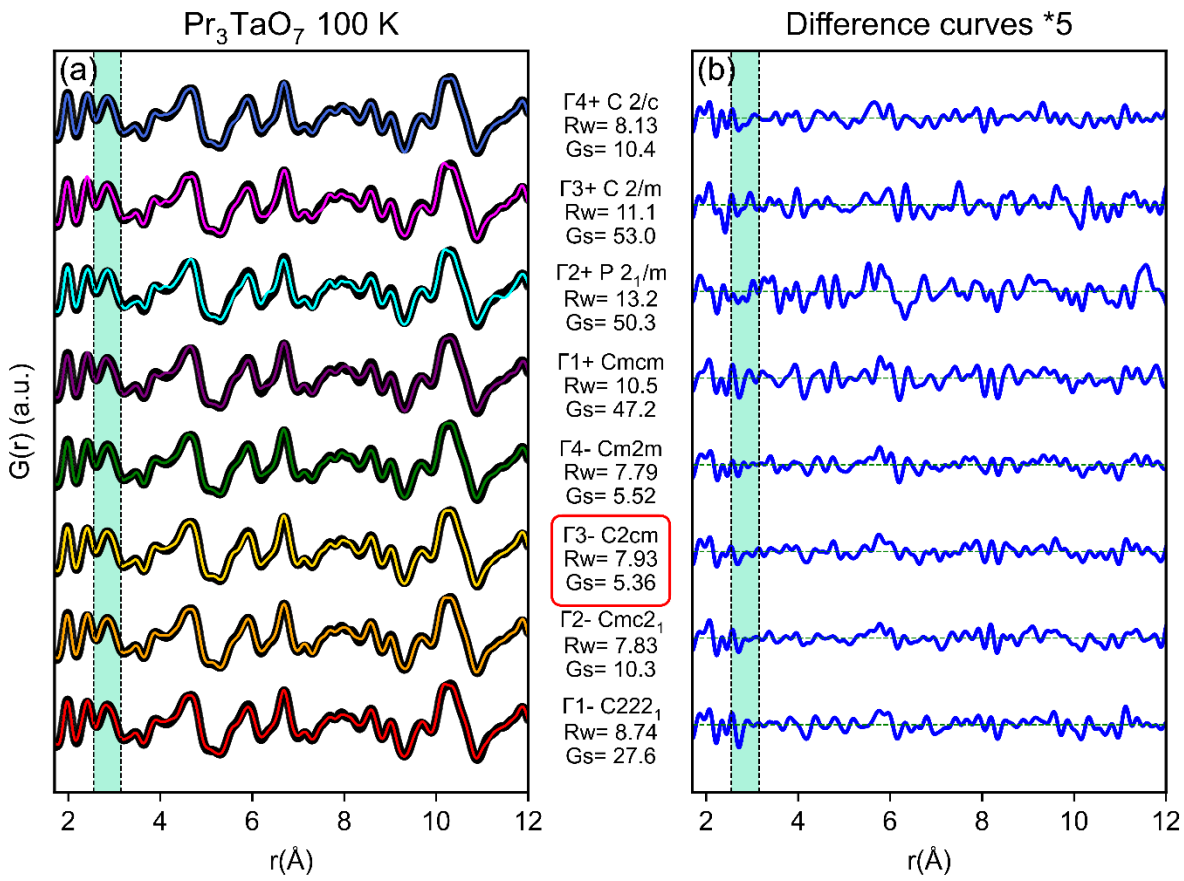

Figure 6: (a) Neutron pair distribution function (PDF) of weberite-type Pr_3TaO_7 measured at 100 K (black circles) and refined with the long-range *Cmcm* space group (purple) and with the models derived at the Brillouin zone center (red, orange, gold, green, cyan, magenta, and royal blue) of *Cmcm*. The four non-centrosymmetric models ($\Gamma_{1\text{-}4}^{-}$) are the bottom curves and the four centrosymmetric models ($\Gamma_{1\text{-}4}^{+}$) are the top curves. (b) Difference curves (multiplied by a factor 5) between as-collected data and respective models in the *r*-range between 1.7 – 12 Å. The turquoise shaded area enclosed by the vertical dashed lines between 2.5 and 3 Å highlights the region most sensitive to the O-O atomic correlations. The red box around the *C2cm* space group highlights the best structural model to describe the PDF of Pr_3TaO_7.

The same systematic PDF refinement procedure was also applied to Ho_3TaO_7 measured at 100 K (**Figure 7**). All models provided reasonable fits. The *Ccmm* structural model used for the long-range diffraction data produced the largest *Rw* value; therefore, it is not a good choice for the short-range structure. Several models do not capture the details of the O-O pair correlations around 2.5 – 3 Å and produce systematically positive residuals in the difference curves. The quantitative *Gs*-factor analysis (**Figure 7**) identifies the Γ_1^- model as the best in terms of uncorrelated regions, followed by the Γ_3^+ (*C2/m*) model. However, close inspection of the Γ_3^+ model reveals that the 7-coordinated Ho cations exhibit unusually large harmonic (U_{ij}) atomic displacement parameters, despite the measurement being performed at 100 K (**Supplementary Figure 5**). The effect is particularly pronounced along the [010] direction, a side effect related to positional coordinates constrained along this direction by the space group symmetry. This effect is not observed for the Γ_1^- (*C222$_1$*) harmonic model: considering that the *C222$_1$* model has also a smaller set of refined parameters (43 for Γ_1- *versus* 50 for Γ_3^+), we conclude that the short-range organization of Ho_3TaO_7 is best described by the non-centrosymmetric *C222$_1$* space group.

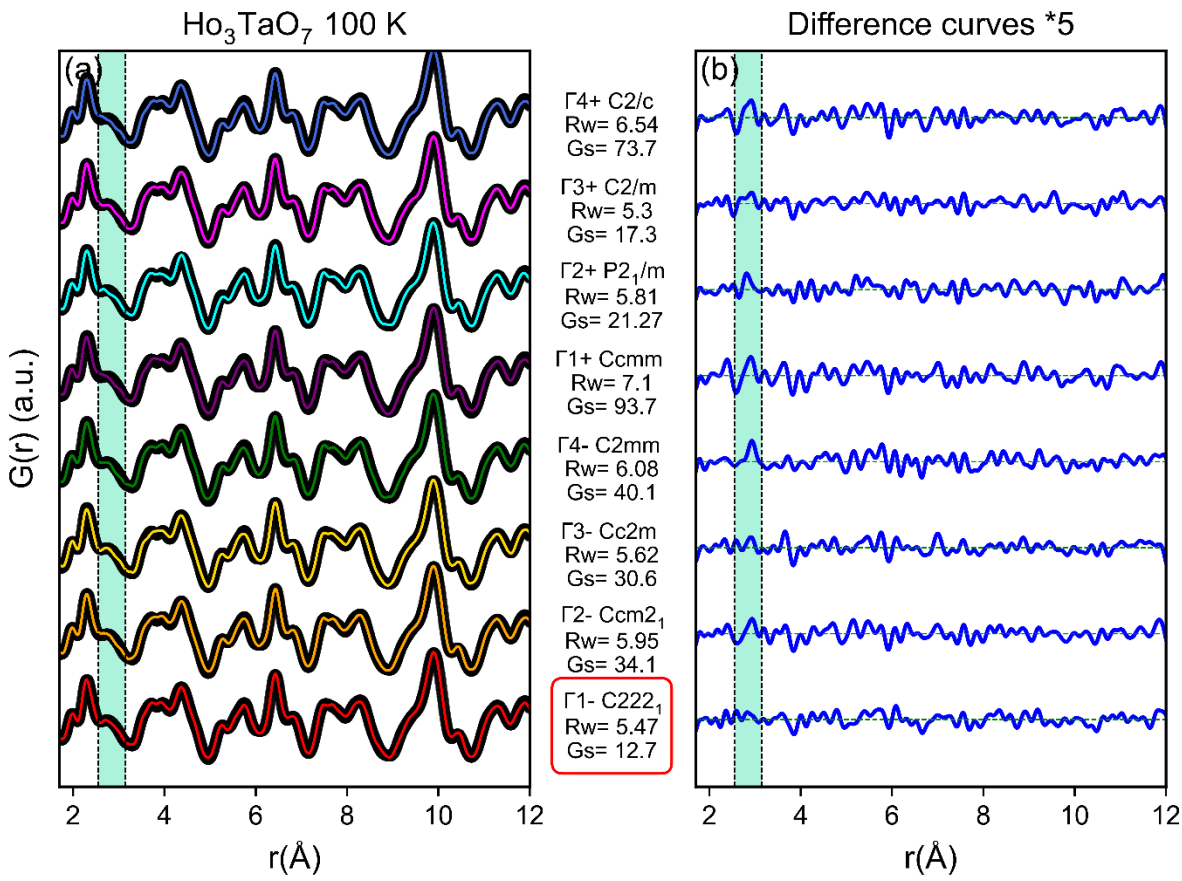

Figure 7: (a) Neutron pair distribution functions of weberite-type Ho_3TaO_7 measured at 100 K and modelled with 7 displacive small-box models in addition to the *Ccmm* long-range space group. Black circles represent the experimental data. Red, orange, gold, green, purple, cyan, magenta and royal blue lines are fits of the respective models. (b) Difference curves (multiplied by a factor 5) between as-collected data and respective models in the *r*-range between 1.7 – 12 Å. The turquoise shaded area enclosed by the vertical dashed lines between 2.5 and 3 Å highlights the region most sensitive to the O-O atomic correlations. The red box around the *C222₁* space group highlights the best structural model to describe the PDF of Ho_3TaO_7.

When comparing the neutron PDF data measured at room temperature refined with the initial long-range symmetry (**Figure 5**) with the improved (low temperature derived) short-range models (**Figure 8**), it is apparent that the average, long-range structure is not the best model for the actual atomic arrangement. This leads to the conclusion that there exists a cross-over between the long-range and short-range symmetry in ordered orthorhombic weberite-type tantalates. Family 1 (Pr_3TaO_7) with *Cmcm* long-range symmetry has a short-range structure that is better described by a *C2cm* local atomic configuration, while family 2 (Tb_3TaO_7 and Ho_3TaO_7) with a *Ccmm* long-range symmetry by a $C222_1$ local atomic configuration. In both cases, a non-centrosymmetric space group is the most suitable model able to fully capture the subtle, local atomic relaxations and distortions, which are particularly evident for the O-O nearest neighbor correlations in the PDFs of the two compounds of family 2. In general, the much-improved fit quality of the $C222_1$ model for structural family 2 reflects the increased degrees of freedom for the Ta cations in TaO_6 octahedra, which is only allowed in non-centrosymmetric space groups (Ta cations are located at the inversion center of the long-range space group structure). Indeed, there are significant displacements of Ta cations observed in the *C2cm* and $C222_1$ models, shifting Ta away from the barycenter of the O anions. In this process, the ADPs of the displaced Ta cations are also satisfactorily reduced in both non-centrosymmetric models according to the expected stiff and tight octahedral environment. The ADPs of the remaining atomic constituents of the structure (Ln cations and O anions) remain unchanged or are slightly reduced.

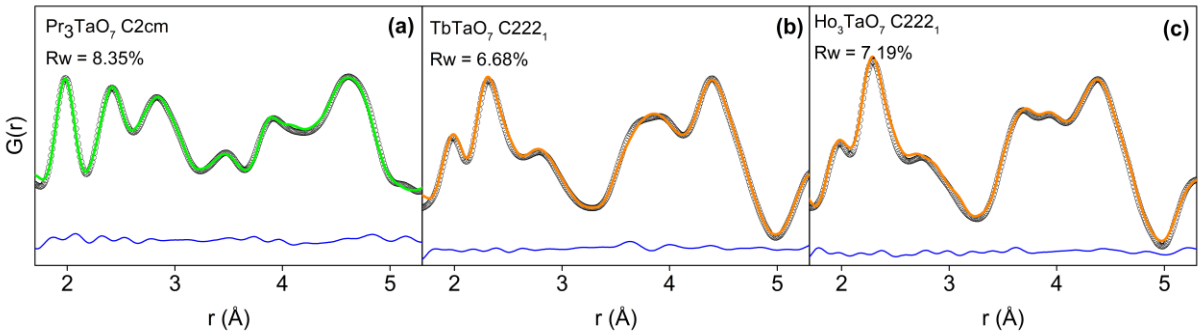

Figure 8: A segment of very local (1.7-5.3 Å) neutron pair distribution functions showing 1st and 2nd nearest neighbor correlations of weberite-type A_3TaO_7 (A=Pr, Tb, Ho) modelled with (**a**) *C2cm* and (**b, c**) *C222₁* space groups, respectively. Black circles represent the experimental data while green and orange curves are fits with the respective models. Difference curves between data and models are displayed in blue.

Small-box analysis of weberite-type compositions with smaller lanthanides (disordered, defect-fluorite structural family)

Discrepancies between the long- and short-range structures (**Figure 4**) are most pronounced in the disordered weberite-type compounds of family 3 with defect-fluorite symmetry (Ln = Ho, Tm and Yb) expressed by unacceptable reliability factors (*Rw* values between 22 and 28%). These findings are consistent with previous observations by King *et al.* (30). The fit quality of the *Fm-3m* model to the PDFs depends on the considered *r*-range, and box-car refinements have been used to determine the extension in real space for which the long-range structure provides an unsatisfactory fit for disordered Ho_3TaO_7, Tm_3TaO_7, and Yb_3TaO_7 (**Figure 9**). Particularly, the low-*r* regions of the PDFs characteristic for the nearest neighbor coordination polyhedra (up to 3 Å) are very poorly described by the *Fm-3m* structural model with *Rw* values up to 30%. The fit quality progressively improves for larger *r* regions but remains poor well beyond the size of the defect-fluorite unit cell. This behavior clearly indicates that these compounds have a distinct local atomic arrangement not represented by the disordered long-range structure.

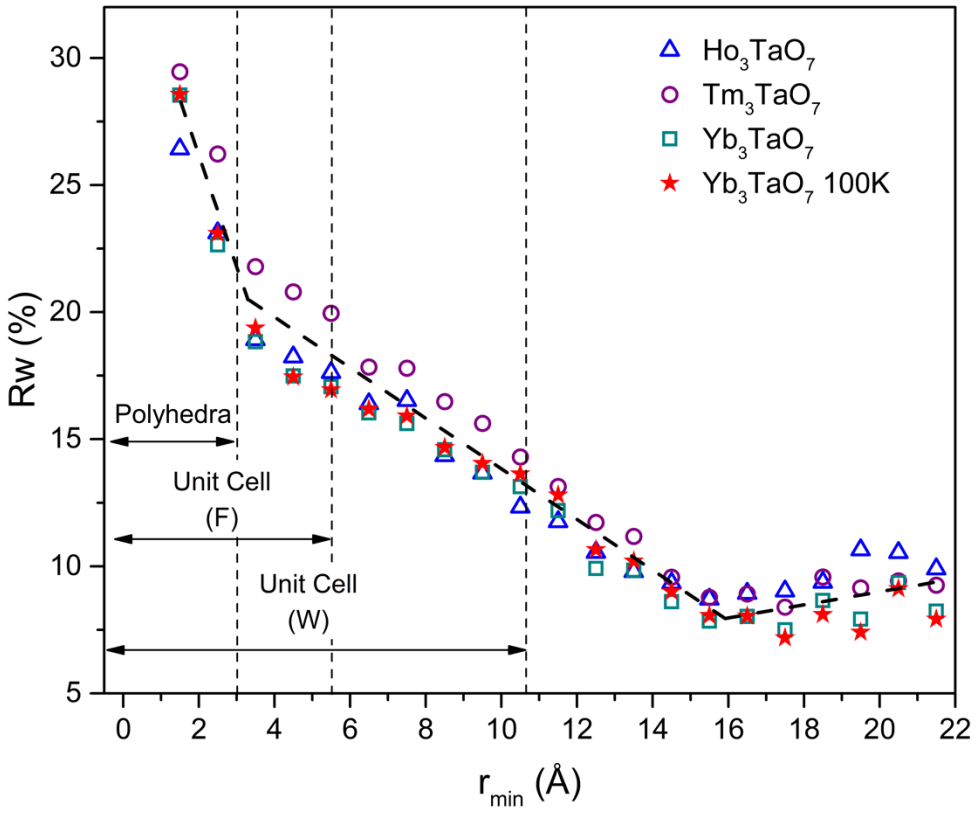

Figure 9: Reliability factors, *Rw*, determined from "boxcar" refinements of neutron PDFs of disordered A_3TaO_7 (A = Ho, Tm, and Yb) measured at room temperature and Yb_3TaO_7 measured at 100 K using the long-range *Fm-3m* structural model. The *x*-axis represents the minimum *r*-value (r_{min}) for each 10.5 Å refinement window and the data points correspond to the *Rw* obtained in each refinement window. The bold black dashed line is to guide the eyes with respect to the *Rw* behavior and the vertical dashed lines represent the characteristic distances corresponding to the polyhedra, the lattice parameter a_F of the defect-fluorite unit cell (F), and the a_W lattice parameter of the weberite-type unit cell (W). The different symbols represent individual compounds of the disordered weberite-type family 3 as labelled in the legend.

Boxcar refinement was performed by monitoring the resulting *R*w values from PDF small-box modeling as a function of a constant *r*-range window (10.5 Å) with increasing minimum fit boundary, r_{min}. The behavior is consistent for all compounds with an initially very high *Rw* value

(r_{min} =1.5 – 3 Å) that gradually decreases until reaching a minimum of approximately 10% for a r_{min} of about ~15 Å (**Figure 9**). This means that the defect-fluorite model provides only a good description of the structure for interatomic distances and pair correlations exceeding 3-4 times the dimension of the cubic defect-fluorite unit cell (approximately 2 times of the conventional orthorhombic weberite-type unit cell). This trend holds even if the PDF was obtained at low temperature as for Yb_3TaO_7 measured at 100 K. Therefore, an improved structural model must be found to describe the short-range structural details below a *r*-range of about ~15 Å.

For all disordered compounds, Yb_3TaO_7 has the most favorable scattering conditions due to its large neutron scattering length of Yb (12.4 fm); thus, the PDF of this sample was used for the most selective analysis of the short-range structure. Based on the boxcar refinements (**Figure 9**), the small-box modeling was limited to a region of *r*-space where the *Fm-3m* long-range model did not provide a good fit quality (1.5 to 12 Å). As alternative structural models for the disordered compounds of family 3, the eight displacive orthorhombic models with tilt system [010], derived from the zone-center representations of the *Ccmm* long-range symmetry (of the neighboring structural family 2), were initially tested. The short-range analysis with these alternative models followed the same approach as described for the ordered weberite-type Ho_3TaO_7 (**Figure 7**). To obtain the best structural model for these disordered atomic configurations, the following approach was adopted: (*i*) the sample was measured at 100 K, where the effect of thermal vibrations is greatly reduced, and (*ii*) the number of allowed thermal parameters was decreased by using only isotropic thermal factors (U_{iso}) to increase the selectivity of the model on the atomic positions. The U_{iso} parameters in each model were set to be distinct for all cation sites and the oxygen sites forming TaO_6 polyhedra and identical for all remaining oxygen sites. This resulted in a smooth convergence of the refinements as shown in **Figure 10a**.

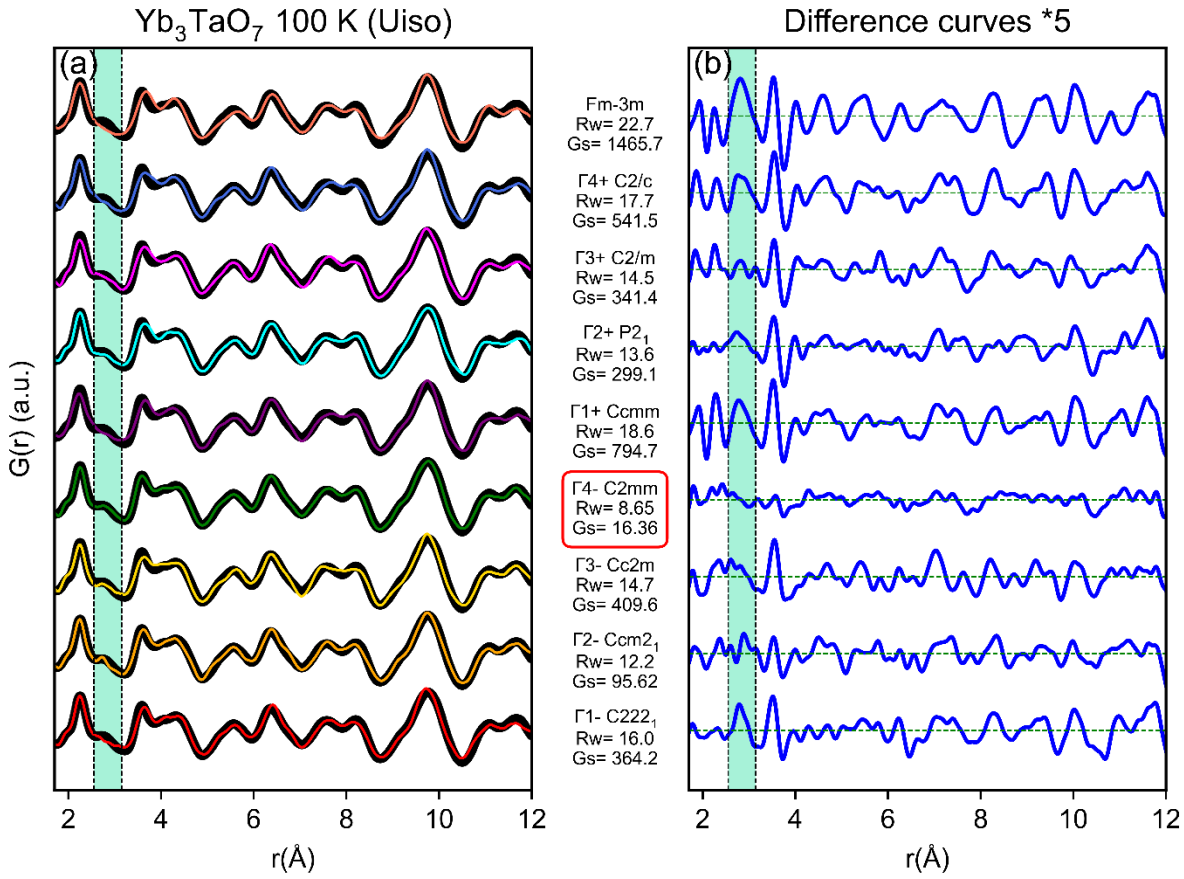

Figure 10: (a) Neutron pair distribution functions of Yb_3TaO_7 measured at 100 K (black circles) and refined with the *Fm-3m* defect-fluorite model (top). The eight alternative models are shown as red, orange, gold, green, purple, cyan, magenta, and royal blue curves. (b) Difference curves (multiplied by a factor 5) between data and models in the *r*-range between 1.7 – 8 Å. The turquoise shaded area enclosed by the vertical dashed lines between 2.5 and 3 Å highlights the region most sensitive to the O-O atomic correlations. The red box around the *C2mm* space group highlights the best structural model to describe the PDF of Yb_3TaO_7.

All alternative lower symmetry models significantly improved the fit quality (*R*w values of 10 – 18.6%). Among these models is the one proposed by King *et al.*, who used $C222_1$ to model the short-range structure of Yb_3TaO_7 (30). However, the best small-box refinements in this study

were obtained with the Γ_2- (*Ccm2₁*) and Γ_4- (*C2mm*) models (*R*w values of 12.2 and 8.65%, respectively), while refinement with Γ_1- produced a significantly higher *R*w value of 16%. As mentioned before, the most accurate model must describe particularly the PDF region (1.5-3.5 Å) representative of the nearest neighbor distances and coordination polyhedra. Careful inspection of the difference curve in the low-*r* region (**Figure 10b)** reveals that all centrosymmetric models, with the exception of Γ_2+ (*P2₁/m*), produce a systematic misfit in the region between 1.5 and 2.5 Å for the Ta-O (first positive residual in PDF) and Yb-O nearest neighbor correlations (second positive residual in PDF). In addition, the O-O nearest neighbor correlations show distinct residuals for these models (shaded region in **Figure 10b**). Overall, the four non-centrosymmetric models agree much better to the data with respect to the Ta-O and Yb-O correlations, but they differ in the description of the O-O correlations. Quantitative analysis of *Gs* confirms that the Γ_4- (*C2mm*) model also has by far the lowest correlated residual among all models. Therefore, we conclude that this is the most accurate model in describing the short-range structure of Yb_3TaO_7. The complete structural information obtained from PDF refinement of 100 K short-range data are summarized in **Supplementary Table 4**.

The use of this non-centrosymmetric space group indicates an inversion center loss at the atomic scale. This space group provides more degrees of freedom and differentiates Ta-O bond lengths, allowing more pronounced distortions of TaO_6 octahedra. Nonetheless, despite this displacive disorder, a high level of occupational order is locally maintained, which contrasts the fully disordered character of the long-range defect-fluorite structure. However, there are still some regions in the PDF that are not fully captured by the *C2mm* model (*e.g.*, feature at 3.9 Å). This suggests that mesoscale polyhedra stacking and ferroelastic boundaries among nanoscale *C2mm*

domains can produce detectable correlations in the PDF, which cannot be described with a simple small-box model.

To test the broader transferability of the newly established model, the PDFs of all three defect-fluorite structured samples (Ho_3TaO_7, Tm_3TaO_7, and Yb_3TaO_7) measured at the room temperature were refined with the same *C2mm* space group over the same *r* region (1.5-12.0 Å). Small box modeling using this model (**Figure 11**) provided excellent agreement to the experimental data with a significant drop in *Rw* values compared to the initial fits with the long-range *Fm-3m* structural model (**Figure 4**). The lower *Rw* value for Yb_3TaO_7 at room temperature compared to low temperature can be explained by the effect of thermal broadening. The overall good agreement, for all disordered samples studied here, leads to the conclusion that the compounds of weberite-type family 3 with a long-range *Fm-3m* structure, are best described by the orthorhombic *C2mm* space group.

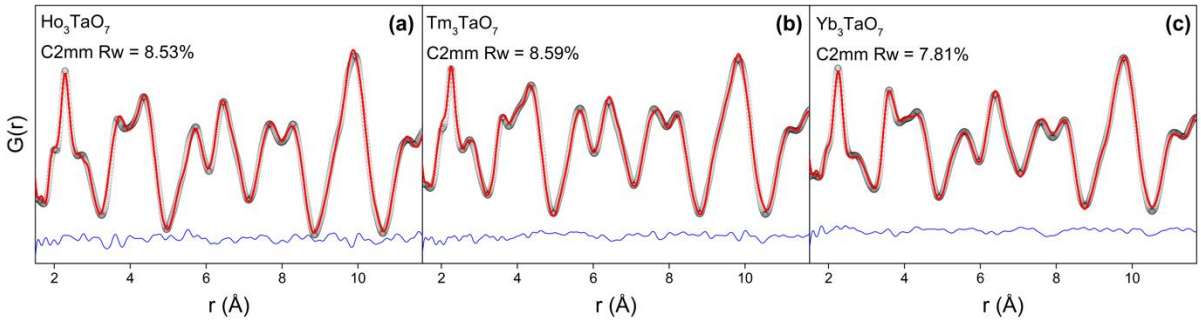

Figure 11: Neutron pair distribution functions (black circles) of disordered Ho_3TaO_7, Tm_3TaO_7, and Yb_3TaO_7 measured at room temperature and modeled (red curves) using the *C2mm* space group derived from PDF refinement of Yb_3TaO_7 measured at 100 K (Fig. 10). The blue curves represent the difference between experimental data and refinement.

The simultaneous characterization of the short-range and long-range structure by total scattering experiments revealed that all studied weberite-type tantalates exhibit some degree of structural heterogeneity across different length scales. In all cases, the space groups, which modeled the diffraction data the best, did not accurately describe the PDFs. Alternative structural models were required to capture the local atomic configurations, an exploration that yielded improved small-box refinements. To summarize this behavior and derive general trends among the three structural families, the *Rw* values of initial and improved PDF models were compared (**Figure 12**). The improved model used for disordered family 3 compounds showed a large *Rw* drop, suggesting that the atomic arrangements in disordered compounds are most distinct from the long-range average structures. The local structure is in fact quite similar to the short-range organization of intermediate lanthanides of family 2 (Tb, Ho) that display an ordered long-range orthorhombic structure. The refinement of the PDFs of family 2 samples with the improved local model showed a more limited decrease of *Rw*. This indicates that the short-range structure of these compounds has only minor deviations from the long-range centrosymmetric model. For the larger lanthanides, Pr_3TaO_7, of the ordered orthorhombic family 1, the reduction in *Rw* values is somewhat larger again as compared with family 2 compounds, suggesting more pronounced deviations of the local atomic arrangement from the long-range centrosymmetric structure. While this *Rw*-value analysis (**Figure 12**) is partially biased by the different neutron scattering lengths of the individual lanthanide elements (ranging from 4.6 fm for Pr to 12.4 fm for Yb), it still highlights the structural complexity across all weberite-type tantalates, showing a strong dependence on chemical composition and characteristics of the long-range structure.

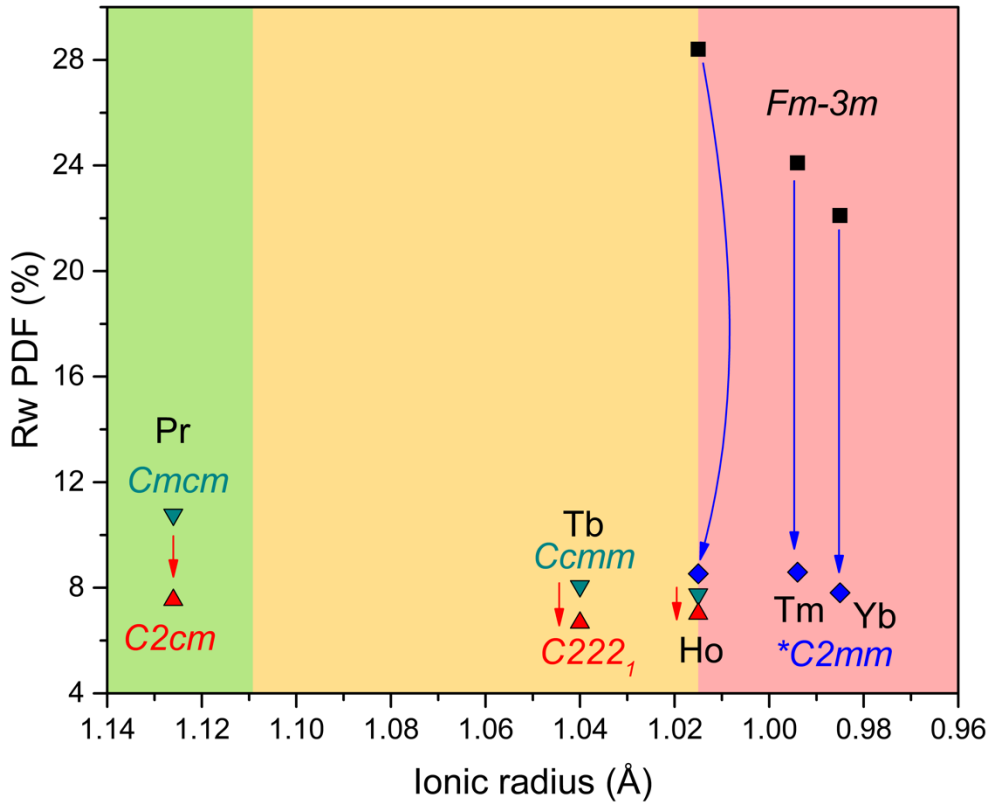

Figure 12: Reliability factors (*Rw*) of neutron PDF refinements of Ln_3TaO_7 compounds displayed as a function of the ionic radius of the Ln cation. *Rw* values based on *Cmcm* and *Ccmm* structural models are shown as downward oriented dark green triangles, and as black squares for *Fm-3m* structural model. *Rw* values based on alternative *C2cm*, *C222₁* models are shown as upward oriented red triangles and as blue chevrons for *C2mm* model respectively. Red and blue arrows denote decrease in *Rw* factors for improved models. Green, yellow and red shaded regions represent the long-range structural families: green = family 1 (*Cmcm*), yellow = family 2 (*Ccmm*), and red = family 3 (*Fm-3m*).

Discussion

Considering the structures of weberite-type tantalates as a derivative of the high-symmetry prototype *Cmmm* structure, provides a unified framework for explaining the findings of this study. The three structural families can be described by two distinct tilt systems, [100] and [010], corresponding to distinct irreducible representations of this prototype structure at the *Z*-point of the Brillouin zone. The two tilt systems were unambiguously determined through analysis of peak extinctions in high-resolution diffraction data. Structural family 1 compounds with large lanthanides (Pr_3TaO_7) exhibit a *Cmcm* long-range structure with the [100] tilt system, while structural family 2 compounds with intermediate lanthanides (Tb_3TaO_7 and ordered Ho_3TaO_7) display the *Ccmm* space group with the [010] tilt system. Only one weberite-type tantalate compound can display both tilt systems: Nd_3TaO_7, at the boundary between families 1 and 2 undergoes a first order semi-reconstructive transition from a low temperature [010] tilt system to a high temperature [100] tilt system as reported in (15). Finally, family 3 compounds with small lanthanides (disordered Ho_3TaO_7, Tm_3TaO_7, and Yb_3TaO_7) with a defect-fluorite structure *Fm-3m* exhibit the same tilt system as structural family 2, but with a very short correlation length. The average tilt angle of TaO_6 octahedra is directly related to the *c*-axis of weberite-type structures. The amplitude of this tilt was extracted using the lattice parameters determined in the present study (neutron total scattering and X-ray diffraction results) and those reported by Wakeshima *et al*. (15). In the case of the defect-fluorite structure, the *c*-axis was reconstructed by using the metric transformation between the two lattices ($a_F\sqrt{2}$). The average tilt angle increases linearly as a function of decreasing ionic radii of the lanthanide ions across all three structural families (**Figure 13, white squares**). While the transition from structural family 2 to family 3 (Ho_3TaO_7) displays a continuous evolution at the macroscopic scale, there is an apparent discontinuity between

families 1 and 2 (Nd_3TaO_7). This is a result of the change in the Ta-O-Ta inter-polyhedra tilt system occurring between the low- and high-temperature polymorphs of Nd_3TaO_7.

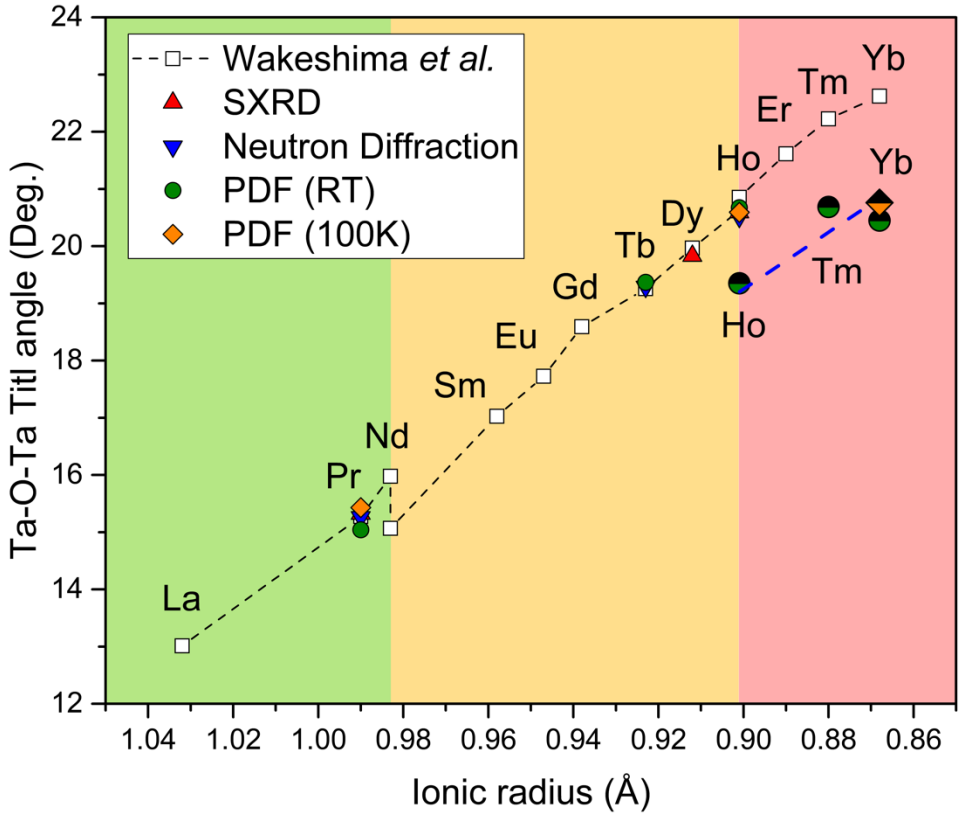

Figure 13: Ta-O-Ta tilt angles between TaO_6 octahedra in Ln_3TaO_7 derived from c-lattice parameters published by Wakeshima *et al.* (15) as a function of ionic radius of the lanthanide cations shown as white squares and connected by a black dashed line. The c-lattice parameter for (long-range) defect-fluorite structured compounds (Ln = Ho-Yb) was estimated as $a_F\sqrt{2}$. Tilt angles determined from c-lattice parameters measured in this study by SXRD and neutron diffraction data (long-range) are shown as red and blue triangles. Tilt angles determined from short-range structures are shown as green spheres for room temperature data and as orange chevrons for 100K data. Fully filled circles and chevrons denote PDF models obtained from ordered compounds (Pr, Tb, Ho) whereas partially filled colored symbols denote models obtained for disordered compounds (Ho, Tm, Yb) with blue dashed line serves as a guide to the eye. Green, yellow and red shaded regions represent the long-range structural families: green = family 1 (*Cmcm*), yellow = family 2 (*Ccmm*), and red = family 3 (*Fm-3m*).

None of these long-range structural models provide an accurate description of the local structure. Improved models were derived for all three families and allowed the description of local tilts and deformations of coordination polyhedra across the entire lanthanide series. The evolution of the tilt angle of TaO_6 octahedra derived from the PDF refinements shows excellent agreement with the results from the long-range analysis for families 1 and 2 at room temperature and low temperature (**Figure 13, colored symbols**). The structure analysis of the PDF data of family 3 allows direct determination of the tilt angle beyond the estimation based on the lattice parameter of the defect-fluorite structure. The evolution of the tilt angle with decreasing ionic radii remains linear for the three compositions of family 3 with no explicit dependence on the sample temperature (**Figure 13, partially filled symbols**); however, there is a distinct discontinuity between families 2 and 3, occurring for the ordered and disordered polymorphs of Ho_3TaO_7. Despite the observed discontinuities, a single slope seems to describe all data.

The systematic increase in tilt angle across the entire series can be explained by the contraction of the lanthanide ionic radii. The linear dependence suggests that rigid TaO_6 octahedra are a good approximation because the tilt angle produces a linear reduction of the available volume for the lanthanide polyhedra. This also explains the two observed discontinuities; the tilt angle is larger for the high-temperature polymorph of Nd_3TaO_7, but is reduced for low-temperature phase, thus maintaining an optimum volume available for the Nd cation. For Ho_3TaO_7, the ordered polymorph has a larger tilt, reducing the volume required for the Ho cation, a configuration that cannot be achieved in the disordered polymorph where the Ho experiences significant positional disorder.

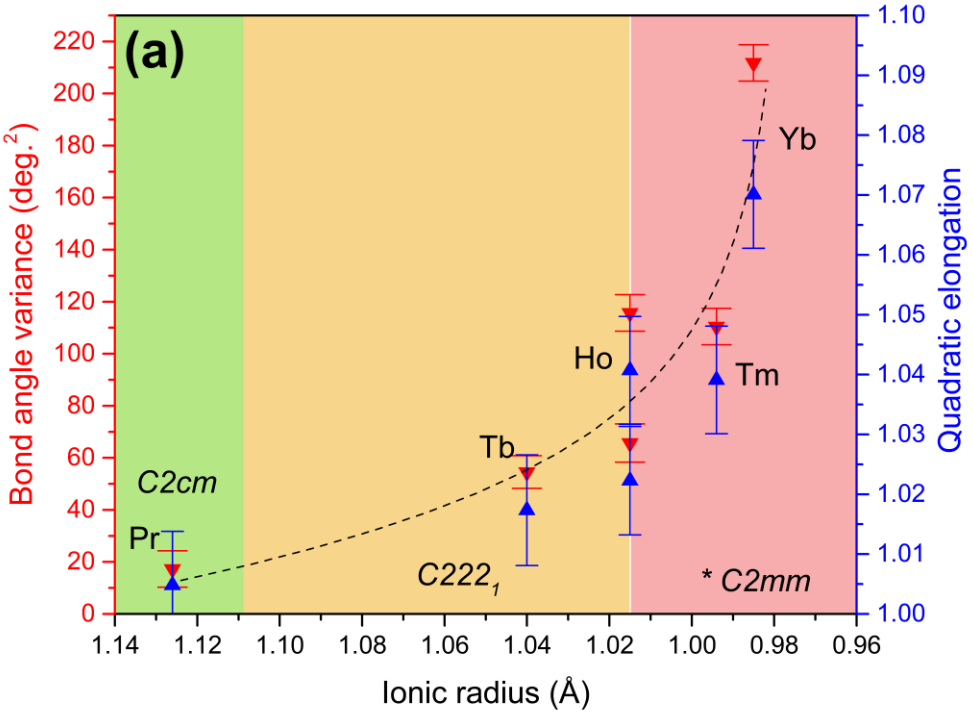
(a)
Bond angle variance (deg.^{2})
Quadratic elongation
Ionic radius (Å)
Pr
Tb
Ho
Tm
Yb
C2cm
C222$_1$
* C2mm

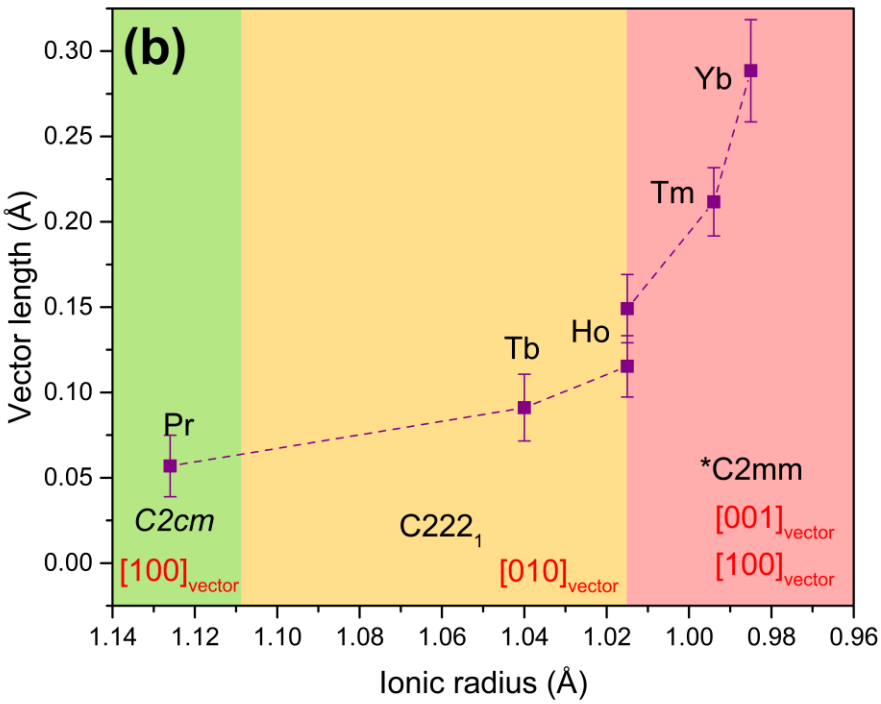
(b)
Vector length (Å)
Ionic radius (Å)
Pr
Tb
Ho
Tm
Yb
C2cm
[100]$_{vector}$
C222$_1$
[010]$_{vector}$
*C2mm
[001]$_{vector}$
[100]$_{vector}$

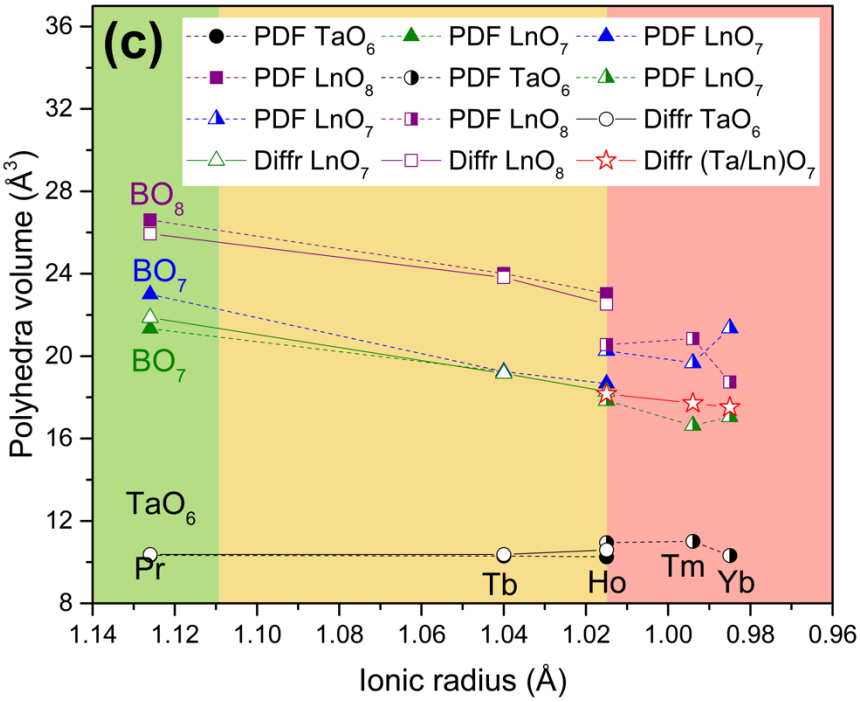

Figure 14: Various polyhedra parameters of Ln_3TaO_7 (Ln = Pr, Tb, Ho, Tm, and Yb) extracted from PDF refinements using *C2cm* (Pr), *C222₁* (Tb, Ho), and *C2mm* (disordered Ho, Tm, Yb) models. (a) Bond angle variance (downward oriented red triangles) and quadratic elongation (upward oriented blue triangles) parameters of TaO_6 octahedra with the dashed black curve serving as a guide to the eyes. (b) Magnitude of the displacement vectors (distance between the Ta position and the O_6 barycenter) and respective vector directions. (c) Respective volumes of TaO_6, BO_7, and BO_8 polyhedra from short-range structures (*C2cm*, *C222₁*, *C2mm*) shown as completely filled symbols for Ln = Pr, Tb, and ordered Ho and as semi-filled symbols for Ln = disordered Ho, Tm, and Yb. Additionally shown as white-filled symbols are the average polyhedra volumes from the long-range structures (*Cmcm*, *Ccmm* and *Fm-3m*). Circles, upward-oriented triangles and squares indicate TaO_6, LnO_7 and LnO_8 polyhedra, respectively, whereas white-filled red stars indicate average $(Ta/Ln)O_7$ polyhedra from long-range *Fm-3m* models. For the ease of visualization, the legend is also shown within the white box above the data, denoting polyhedra from long-range diffraction and short-range PDF models as '*Diffr*' and '*PDF*', respectively. Green, yellow, and red shaded regions represent the three weberite-type tantalate long-range families with green (family 1, *Cmcm*), yellow (family 2, *Ccmm*), and red (family 3, *Fm-3m*). The error bars in (a) represent propagated uncertainties from quadratic elongation and bond angle variance formulas, while in (b), uncertainties are calculated by the VESTA crystallographic software.

For the discussion of the octahedral tilt, TaO_6 octahedra were approximated as rigid units; however, small internal distortions may occur that can be assessed through analysis of the short-range structure. Two parameters are important to describe such distortions: the bond-angle variance and the quadratic elongation (36), which were both determined by atomic positions from the PDFs for all compounds (**Figure 14a**). The TaO_6 octahedra in family 1 compounds (Pr_3TaO_7) have six almost identical Ta-O bonds, and therefore, an extremely small value of quadratic elongation (15), but slightly different O-Ta-O angles (whose distributions are described by the bond angle variance), a feature characteristic of a pure trigonal distortion. For family 2 (Tb_3TaO_7 and ordered Ho_3TaO_7), the Ta-O bonds display larger trigonal distortions, and a tetragonal distortion also develops with the Ta-O bond lengths splitting into three pairs of distances for these compounds. At the boundary between family 2 and family 3 there appears another discontinuity, which is apparent in both distortion parameters of the ordered and disordered polymorphs of Ho_3TaO_7. For family 3 compounds (disordered Ho_3TaO_7, Tm_3TaO_7, and Yb_3TaO_7) both parameters further increase with decreasing ionic radii of the lanthanide cations, mirroring the behavior already observed for the octahedral tilts (**Figure 13**).

While the underlying mechanisms of these distortions are not fully understood, this seems to be a secondary effect of the octahedral tilts; for family 3, the larger amplitudes can be related to the loss of long-range order. The distortion of the TaO_6 octahedra might be explained by a pseudo-Jahn-Teller type mechanism as observed in perovskite compounds (37), because the Ta^{5+} cations in an octahedron have d^0 electronic configuration, known to promote off-center displacements. From this analysis, such octahedral distortions are significant in weberite-type tantalates and

suggest an increasing covalent bonding character of the corner-shared TaO_6 framework in compounds with smaller lanthanide cations. Weberite-type compounds have often been studied for their magnetic properties (15); however, the short-range analysis reveals the ferroelectric character of the TaO_6 octahedra due to the non-centrosymmetric nature of the local atomic arrangement. It would be therefore more appropriate to classify these compounds as multiferroic systems.

The off-center displacements of the Ta^{5+} cations within the coordination polyhedron can be precisely captured by the dipolar vector defining the position of the geometric center of mass of the O_6 group of anions relative to the actual Ta position (**Figure 14b**). Following the same trend of the distortion parameters (**Figure 14a**), the dipolar vector increases slightly from Pr_3TaO_7 to ordered Ho_3TaO_7, then followed by a sharp increase for disordered Ho_3TaO_7, a trend which extends to the other disordered compounds of family 3.

All changes to the rigid TaO_6 framework (tilts and distortions) are likely to impact the other polyhedra. Since LnO_7 and LnO8 are irregular, it is hard to develop equivalent distortion parameters to describe their changes; therefore, we analyzed the changes in polyhedra volumes measured across all structural families as a function of ionic radii (**Figure 14c**) for both local short-range (colored symbols) and long-range (white symbols) structures. As expected, the TaO_6 octahedra experience no significant change across the series, being the most rigid element of the structure. On the other hand, LnO_8 and LnO_7 polyhedra show a monotonic decrease of their volumes as a function of Ln ionic radii, with LnO_8 decreasing more rapidly than LnO_7, a trend accelerating in disordered compounds. No significant discrepancy between short-range and long-range polyhedra volume is observed in ordered compounds, whereas at the frontier between family 2 and 3, disordered compounds display an abrupt change in volume leading to smaller polyhedra

than what can be estimated from long-range trends. Moreover, in *C2mm* local structure (Γ_4-) there are two independent LnO_7 polyhedra: the volume of one of them converges to the volume of LnO_8, whereas the other one is consistently smaller.

Three different space groups were used to model the local structure of all weberite-type tantalates using small-box refinement of the PDFs. This is required to obtain an accurate description of the atomic arrangement of each compound. Nevertheless, the changes across the short-range structure are more gradual and are captured by the cooperative tilts and distortions of the coordination polyhedra (**Figures 13 and 14**). The spatial extent of these modifications over macroscopic length scales is highly dependent on the ionic radii of the lanthanide cations and determines the apparent symmetry of the long-range structure. The two observed tilt systems, which were described as instabilities of the *Cmmm* prototype structure, explain the two observed long-range symmetries of family 1 and 2. For a given tilt angle, tilt system [010] of family 2 is more effective in achieving the necessary polyhedra volume reduction to accommodate the lanthanide cations in the structure. With further increase in tilt, dipolar contributions of the Ta cations also increase, competing energetically with the tilts. Above a given threshold in lanthanide ionic radii, the dipolar energy begins to dominate and prevents a long-range tilt organization, leading to a long-range disordered structure. This marks the transition between families 2 and 3. For Ho_3TaO_7, this cooperative ordering of the dipoles depends on the annealing conditions, which explains the existence of the ordered and disordered polymorphs.

The rank ratio of the space groups of the local structure and long-range structure provides the number of domain variants required to achieve the apparent long-range symmetry (38,39). The long-range structure is the configurational average of these correlated local domain variants (40). For example, in structural family 1, the long-range space group is *Cmcm*, while *C2cm* was used to

describe the short-range structure; therefore, only two variants exist as a result of the loss of the mirror plane. In family 2 (long-range *Ccmm*, short-range $C222_1$), two variants also exist, but they are related to each other by the loss of the inversion center. In both cases, configurational averaging of the two variants yields the ordered long-range structure. For family 3 (long-range *Fm-3m*, short-range *C2mm*), 96 variants are involved in the configurational average that forms the disordered defect-fluorite long-range structure since the space groups belong to different crystal systems (orthorhombic and cubic). It is interesting to note, that only Y_3TaO_7 is fully described by the $C222_1$ space group at any length-scale and therefore no configurational averaging is required (16,22).

All of these structural descriptions and underlying effects can be summarized in the following manner: the monotonic decrease Ln ionic radius dictates the formation of three long-range structural families. Family displays a [100] tilt of Ta-O-Ta chains, while structural family 2 displays a [010] tilt and both ordered structures retain the same motif of TaO_6, LnO_7, and LnO_8 polyhedra. In the structural family 3 with defect-fluorite structure, these polyhedra and not distinguishable and tilt definition is lost. Across the structural family 1, the Ln ionic radius decreases, which causes a monotonic contraction of the unit cell, accompanied by the increase of [100] tilt, linked with the c-lattice dimension. The [100] tilt becomes incompatible with the ionic radius of Nd cation, and Nd_3TaO_7 displays a semi-reconstructive first order phase transition, from [100] to [010] tilt systems, which results in a discontinuity in tilt angles for Nd_3TaO_7. As Ln ionic radius continues to decrease, the respective unit cell volumes continue to contact monotonically and Ln cations smaller than Nd adopt [010] tilt system instead, to counteract this behavior. The decrease of orthorhombic unit cell volumes, and especially the 'rigid' c-lattice parameter, causes a monotonic increase of the [010] tilt, reaching maximum for the Ho_3TaO_7 compound. A polymorph of Ho_3TaO_7 and Ln cations smaller than Ho display a disordered structure with almost

no structural information. The alternative short-range structures are identified for all three families to counter this issue and to characterize the following structural features: (i) an inter-polyhedra loss of inversion center, governed by increasing polarizability of Ta cation (ii) corresponding distortions of polyhedra across the compositional series, (iii) Ta-O-Ta tilt angle, an intra-polyhedral character and (iv) the respective sizes of 'rigid' TaO_6, 'soft' LnO_8 and LnO_7 polyhedra. Within these short-range structures, several trends can be observed. The decreasing ionic radius of Ln cation results in (i) an increasing polarization of Ta, thus an increasing offset of Ta cation from TaO_6 barycenter, which in turn dictates the necessity of non-centrosymmetric space groups to describe the local organization, (ii) an increasing amount of local trigonal (Pr) and then both trigonal and tetragonal (Tb-Yb) distortions across the series, (iii) increasing Ta-O-Ta tilt angle, necessary to compensate the decrease of c-lattice parameter and (iv), a monotonic decrease of polyhedra size across the series. As all of these effects are accumulated, the structure becomes unable to compensate for accumulated distortions and collapses to a long-range defect-fluorite configuration for a smaller Ln. Locally, this effects progresses even across structural family 3, as Ta-O-Ta, polyhedra distortions and increased polarization of Ta cation mark a consistent trend across the local organization.

It remains to be shown whether the findings of this study on weberite-type tantalates have implications to other weberite-type compounds, such as niobates (Ln_3NbO_7) and antimonates (Ln_3SbO_7). The electron affinity increases in the sequence Ta^{5+} - Nb^{5+} - V^{5+} and Jorgensen *et al.* (41) has discussed the nephelauxetic effect in several octahedral compounds establishing that covalency, described by the formation of molecular orbitals from the metal ion orbitals and the orbitals of the surrounding oxygen anions, increases in the sequence 5*d*-4*d*-3*d*. The Nb^{5+} and Ta^{5+} cations have no *d* electrons, whereas the Sb^{5+} cation has a completely filled *d* shell. The structural

differences between mixed metal oxides containing Nb^{5+}, Sb^{5+}, and Ta^{5+} cations can be qualitatively understood by the different metal interactions, which are very effective for Nb^{5+}, not effective for Sb^{5+}, and only weakly effective for Ta^{5+} (42). Therefore, it can be expected that displacements are strongly enhanced in Nb^{5+}, weaker in Ta^{5+}, and unfavorable for Sb^{5+}. The expected ferroelectric character should then be distinct in the three series of weberite-type oxides as well as the competitive magnetic interactions.

The complex structural behavior with ordered local atomic configurations within a highly disordered long-range structure found in this study for family 3 appears to be a broader phenomenon. A similar behavior was reported before for disordered, defect-fluorite structured $A_2B_2O_7$ pyrochlore (32,33,40) , inverse AB_2O_4 spinel (43), and $A_4B_3O_{12}$ delta phase (44). These results show that atomic arrangements describing the ground state of a material may differ from that derived from analysis of X-ray diffraction data providing information on the long-range structure. The discrepancy between short- and long-range structures appears to be most pronounced for disordered systems. A more comprehensive multi-scale analysis is therefore required to accurately describe the structure-property relations in complex oxides.

Conclusion

This study revealed that lanthanide-bearing weberite-type tantalates exhibit three distinct long-range structures over the range of lanthanide ionic radii. Structural models were derived based on high-resolution, low-temperature X-ray and neutron diffraction characterization. Family 1 compounds (Pr_3TaO_7) have a *Cmcm* structure, represented by systematic TaO_6 octahedral tilt along [100]. The structure of family 2 compounds was reassessed; the members of family 2 (Tb_3TaO_7 and Ho_3TaO_7) display a *Ccmm* structure, for which the octahedral tilt is along [010]. Family 3 compounds (disordered Ho_3TaO_7, Tm_3TaO_7, and Yb_3TaO_7) have a disordered, defect-fluorite *Fm-3m* structure with no long-range tilt system. However, analysis of the short-range structure by means of neutron PDF analysis revealed that each long-range structure is the result of configurational averaging of local atomic domains with distinct displacements and orientations. The derived structural models for the short-range structure, best described for the three families by non-centrosymmetric *C2cm*, $C222_1$, *C2mm* space groups, respectively, are the true ground states that accurately capture all atomic relaxations, tilts, and distortions. All of these effects are the result of an increased local polarization of Ta cation: the local loss of inversion center, which results in a distortion of polyhedra and progresses monotonically across the series. When the critical quantity of local distortions is acquired, the system experiences a frustration, leading to a change in the direction of the octahedral tilt system, which explains the long-range transition between families 1 and 2. Furthermore, the dipolar interactions with increasing tilt angles are responsible for the loss of long-range order and the transition to family 3. Detailed knowledge of this atomic-scale structural behavior is essential to fully describe the multiferroic character of these compounds. The structural heterogeneity across multiple length scales, particularly pronounced in long-range disordered compounds, may have also implications on other physical properties at the

equilibrium and out-of-equilibrium (*e.g.*, thermomechanical gradients, mass-transport, and irradiation environments) as domain boundaries and interfaces can lead to the formation of a percolating network capable of accommodating large concentrations of point defects.

Declaration of Competing Interest:

The authors declare that they have no known competing financial interests or personal relationships that could have appeared to influence the work reported in this paper.

Author Contributions: I.M.G. and M.L. conceived and designed the study. C.O., I.M.G. provided samples for the study. I.M.G., E.C.O, M.T., Q.Z., J.N. and M.E. performed the neutron total scattering experiments and analyzed the data. I.M.G., D.S., and D.O. performed the X-ray synchrotron diffraction experiments and analyzed the data. G.B. performed the Brillouin zone center calculations. R.C.E. provided crystallographic assessment. I.M.G., G.B., E.C.O. and M.L. interpreted the data. I.M.G. drafted the manuscript with the critical review by all authors.

Acknowledgements:

This work was supported by the U.S. Department of Energy, Office of Science, Basic Energy Sciences, under Award DE-SC0020321. Partial support was provided by the Joint PhD Programme of Université Paris-Saclay as part of the *Investissements d'Avenir* program, grant number ANR-11-IDEX-003. This work was also supported by the U.S. Department of Energy, Office of Science, Basic Energy Sciences, under the SCGSR fellowship program. The SCGSR program is administered by the Oak Ridge Institute for Science and Education for the DOE under contract number DESC0014664. This research used resources at the Spallation Neutron Source, a DOE Office of Science User Facility operated by the Oak Ridge National Laboratory. These experiments and analyses were supported by the U.S. Department of Energy (DOE) Office of Fusion Energy Sciences under Contract No. DE-SC0018322 with the Research Foundation for the State University of New York at Stony Brook. This research used resources at the Pair Distribution Function Beamline of the National Synchrotron Light Source II, a U.S. Department of Energy (DOE) Office of Science User Facility operated for the DOE Office of Science by Brookhaven National Laboratory under Contract No. DE-SC0012704.

Authors express their appreciation to Mason King for his support regarding sample synthesis.

References

1. Cai L, Nino JC. Complex ceramic structures. I. Weberites. Acta Crystallogr Sect B Struct Sci. 2009;65(3):269–90.
2. Linda Francis T, Prabhakar Rao P, Mahesh SK, Sreena TS, Parvathi Babu S. Effect of host structure on the photoluminescence properties of Ln3TaO7:Eu3+ red phosphors. Opt Mater (Amst). 2016;52:134–43.
3. Gómez-García JF, Bucio L, Tavizon G. Dy3TaO7 A stoichiometric spin glass and the effect of disorder via chemical substitution in the Dy3−xYxTaO7 ($0 \leq x \leq 3$) solid solution. J Solid State Chem. 2018;257(2017):49–57.
4. Gomez-Garcia JF, Escudero R, Tavizon G. Spin glass behavior in the Dy3-xY xTaO7 ($0 \leq x \leq 1$) system. J Solid State Chem. 2014;217:42–9.
5. Abe R, Higashi M, Zou Z, Sayama K, Abe Y, Arakawa H. Photocatalytic water splitting into H2 and O2 over R3TaO7 and R3NbO7 (R = Y, Yb, Gd, La): Effect of crystal structure on photocatalytic activity. J Phys Chem B. 2004;108(3):811–4.
6. Abe R, Higashi M, Sayama K, Abe Y, Sugihara H. Photocatalytic activity of R3MO7 and R 2Ti2O7 (R = Y, Gd, La; M = Nb, Ta) for water splitting into H2 and O2. J Phys Chem B. 2006;110(5):2219–26.
7. Subramani T, Navrotsky A. Energetics of Formation and Disordering in Rare Earth Weberite RE3TaO7 Materials. Inorg Chem. 2019;58(23):16126–33.
8. Cai L, Denev S, Gopalan V, Nino JC. Phase transition in weberite-type Gd3NbO7. J Am Ceram Soc. 2010;93(3):875–80.
9. Sugihara H, Abe Y, Higashi M, Abe R, Sayama K. Photocatalytic Activity of R 3 MO 7 and R 2 Ti 2 O 7 (R = Y, Gd, La; M = Nb, Ta) for Water Splitting into H 2 and O 2 . J Phys Chem B. 2006;110(5):2219–26.
10. Preux N, Rolle A, Merlin C, Benamira M, Malys M, Estournes C, et al. La3TaO7 derivatives with Weberite structure type: Possible electrolytes for solid oxide fuel cells and high temperature electrolysers. Comptes Rendus Chim. 2010;13(11):1351–8.
11. Wu F, Wu P, Zong R, Feng J. Investigation on thermo-physical and mechanical properties of Dy3(Ta1-xNbx)O7 ceramics with order-disorder transition. Ceram Int. 2019;45(12):15705–10.
12. Wu F, Wu P, Chen L, Feng J. Structure and thermal properties of Al 2 O 3 -doped Gd 3 TaO 7 as potential thermal barrier coating. J Eur Ceram Soc. 2019;39(6):2210–4.
13. Wakeshima M, Hinatsu Y. Magnetic properties and structural transitions of orthorhombic fluorite-related compounds Ln3MO7 (Ln=rare earths, M=transition metals). J Solid State Chem. 2010;183(11):2681–8.
14. Vente JF, Helmholdt RB, Ijdo DJW. The structure and magnetic properties of Pr3MO7 with M = Nb, Ta, and Sb. Vol. 108, Journal of Solid State Chemistry. 1994. p. 18–23.

15. Wakeshima M, Nishimine H, Hinatsu Y. Crystal structures and magnetic properties of rare earth tantalates RE 3TaO7 (Re = rare earths). J Phys Condens Matter. 2004;16(23):4103–20.

16. Allpress JG, Rossell HJ. Fluorite-related phases Ln3MO7, Ln = rare earth, Y, or Sc, M = Nb, Sb, or Ta. I. Crystal chemistry. J Solid State Chem. 1979;27(1):105–14.

17. Fu WT, IJdo DJW. On the crystal structures of Ln3MO7 (Ln=Nd, Sm, Y and M=Sb, Ta)-Rietveld refinement using X-ray powder diffraction data. J Solid State Chem. 2009;182(9):2451–5.

18. Rooksby HP, White EAD. Rare-Earth Niobates and TantaIates of Defect Fluorite- and Weberite-Type Structures. J Am Ceram Soc. 1964;47(2):94–6.

19. Nath DK. Synthesis of Rare Earth Antimonate Pyrochlores and Cathodoluminescence of Europium(3+) in 3Gd2O3 Sb2O5. Inorg Chem. 1970;9(12):2714–8.

20. Rossell HJ. Fluorite-Related Phases Ln_3MO_7 , Ln = Rare Earth , Y , or SC , M = Nb . Sb , or Ta III. Structure of non-stoichiometric Y_3TaO_7 phase. J Solid State Chem. 1979;27:287–92.

21. Rossell HJ. Fluorite-Related Sb , or Ta II . Structure Phases LnMO7, Ln = Rare Earth , Y or SC , M = Nb , Sb, or Ta. J Solid State Chem. 1979;122:115–22.

22. Gussev IM, O'Quinn EC, Baldinozzi G, Neuefeind J, Ewing RC, Zhang F, et al. Local order of orthorhombic weberite-type Y3TaO7 as determined by neutron total scattering and density functional theory calculations☆. Acta Mater. 2020;196:704–9.

23. Huq A, Kirkham M, Peterson PF, Hodges JP, Whitfield PS, Page K, et al. POWGEN: Rebuild of a third-generation powder diffractometer at the Spallation Neutron Source. J Appl Crystallogr. 2019;52:1189–201.

24. Neuefeind J, Feygenson M, Carruth J, Hoffmann R, Chipley KK. The Nanoscale Ordered Materials Diffractometer NOMAD at the Spallation Neutron Source SNS. Nucl Instruments Methods Phys Res Sect B Beam Interact with Mater Atoms. 2012;287:68–75.

25. Toby BH. EXPGUI, a graphical user interface for GSAS. J Appl Crystallogr. 2001 Apr;34(2):210–3.

26. Toby BH, Von Dreele RB. GSAS-II: The genesis of a modern open-source all purpose crystallography software package. J Appl Crystallogr. 2013;46(2):544–9.

27. Božin ES, Billinge SJL, Proffen T, Farrow CL, Juhas P, Bryndin D, et al. PDFfit2 and PDFgui: computer programs for studying nanostructure in crystals. J Phys Condens Matter. 2007;19(33):335219.

28. Momma K, Izumi F. VESTA 3 for three-dimensional visualization of crystal, volumetric and morphology data. J Appl Crystallogr. 2011;44(6):1272–6.

29. Berar JF, Lelann P. E.S.D.'s and estimated probable error obtained in rietveld refinements with local correlations. J Appl Crystallogr. 1991;24(pt 1):1–5.

30. King G, Thompson CM, Greedan JE, Llobet A. Local structure of the vacancy disordered

fluorite Yb3TaO 7 from neutron total scattering. J Mater Chem A. 2013;1(35):10487–94.

31. Shamblin J, Zhang F, Ewing RC, Bosbach D, Tracy CL, Finkeldei S, et al. Probing disorder in isometric pyrochlore and related complex oxides. Nat Mater. 2016;15(5):507–11.

32. Shamblin J, Tracy CL, Palomares RI, O'Quinn EC, Ewing RC, Neuefeind J, et al. Similar local order in disordered fluorite and aperiodic pyrochlore structures. Acta Mater. 2018;144:60–7.

33. Drey DL, O'Quinn EC, Subramani T, Lilova K, Baldinozzi G, Gussev IM, et al. Disorder in Ho2Ti2−xZrxO7: pyrochlore to defect fluorite solid solution series. RSC Adv. 2020;10(57):34632–50.

34. O'Quinn EC, Tracy CL, Cureton WF, Sachan R, Neuefeind JC, Trautmann C, et al. Multi-scale investigation of heterogeneous swift heavy ion tracks in stannate pyrochlore. J Mater Chem A. 2021;9(31):16982–97.

35. Astaph'ev A V, Sirotinkin VP, Stephanovich SY. Phase transitions in the compounds Ln3NbO7(Ln=Sm-Gd) with fluorite-like structure. Kristallografiya. 1985;30(3):603–4.

36. Robinson K., Gibbs G. V. RPH. Quadratic Elongation: A Quantitative Measure of Distortion in Coordination Polyhedra. Science (80-). 1971;172:567.

37. Spaldin NA. Multiferroics: Past, present, and future. MRS Bull. 2017;42(5):385–9.

38. Aizu K. Possible species of ferromagnetic, ferroelectric, and ferroelastic crystals. Phys Rev B. 1970;2(3):754–72.

39. Neder RB, Frey F, Schulz H. Diffraction theory for diffuse scattering by correlated microdomains in materials with several atoms per unit cell. Acta Crystallogr Sect A. 1990;46(10):792–8.

40. O'Quinn EC, Sickafus KE, Ewing RC, Baldinozzi G, Neuefeind JC, Tucker MG, et al. Predicting short-range order and correlated phenomena in disordered crystalline materials. Sci Adv. 2020;6(35).

41. C. K. Jorgensen. Absorption Spectra and Chemical Bonding in Complexes. Pergamon Press. 1962;147(360):310–2.

42. Blasse G. Qualitative approach to the structural differences between some mixed metal oxides containing Sb5+, Nb5+ and Ta5+. J Inorg Nucl Chem. 1964;26(7):1191–9.

43. O'Quinn EC, Shamblin J, Perlov B, Ewing RC, Neuefeind J, Feygenson M, et al. Inversion in Mg 1– x Ni x Al 2 O 4 Spinel: New Insight into Local Structure. J Am Chem Soc. 2017;139(30):10395–402.

44. Baldinozzi, G., Casillas-Trujillo, L., Patel MK et al. Structural complexity of Y6BO12 fluorite-related ternary oxides. MRS Adv. 2021;6:107–11.

Supplementary information:

Supplementary Table 1: Starting values for the Ln_3TaO_7 prototype *Cmmm* (65) structure.

Ln_3TbO_7		**a (Å)**	**b (Å)**	**c (Å)**
Cmmm		10.49940	7.42422	3.71211
Atom	**Wyckoff Site**	**x**	**y**	**z**
Ta1	2a	0	0	0
Ln1	2b	0	0.5	0
Ln2	4f	0.25	0.25	0.5
O1	8p	0.37388	0.29953	0
O2	2d	0	0	0.5
O3	4h	0.125	0.5	0.5

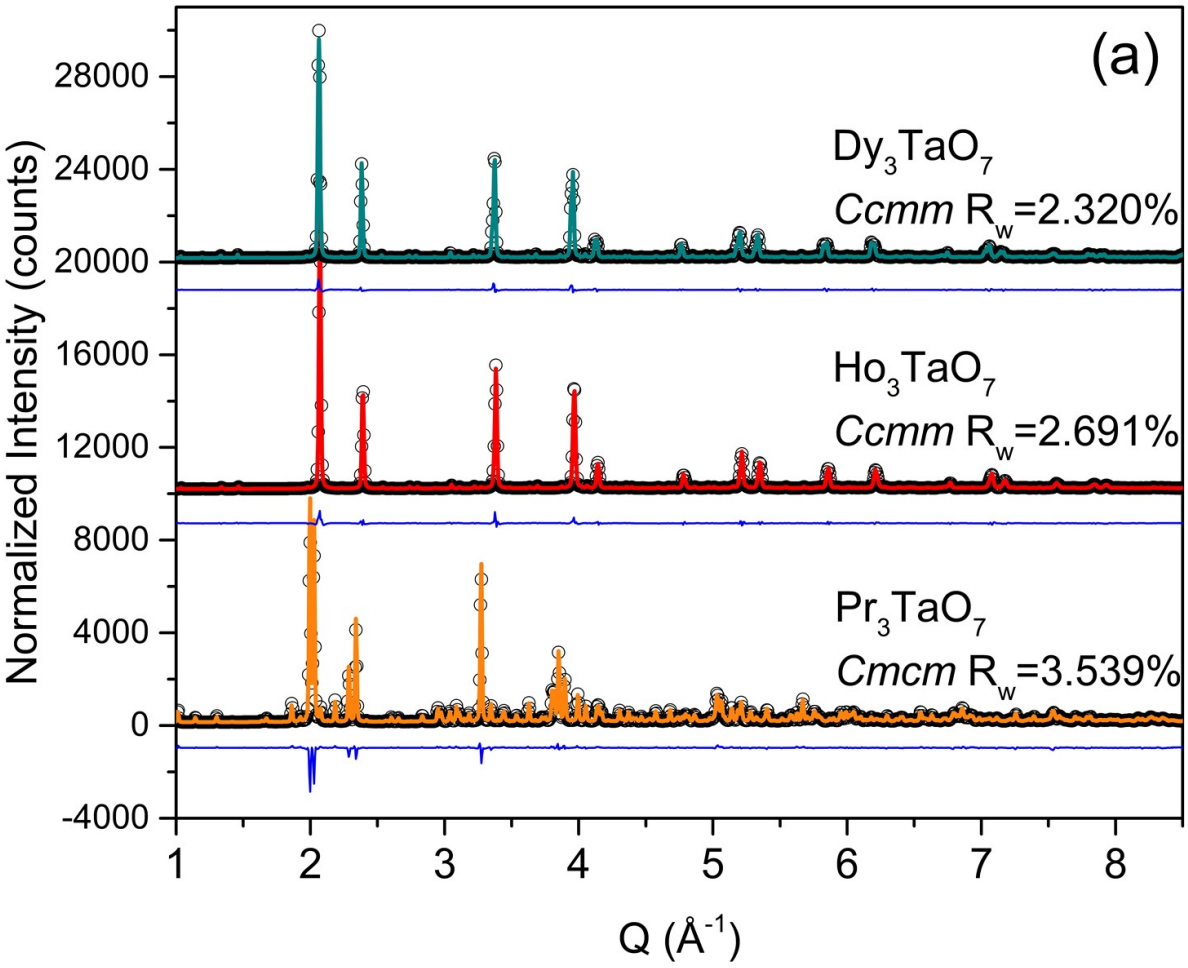
(a)
Dy3TaO7
Ccmm Rw=2.320%
Ho3TaO7
Ccmm Rw=2.691%
Pr3TaO7
Cmcm Rw=3.539%
Normalized Intensity (counts)
Q (Å-1)
28000
24000
20000
16000
12000
8000
4000
0
-4000
1
2
3
4
5
6
7
8

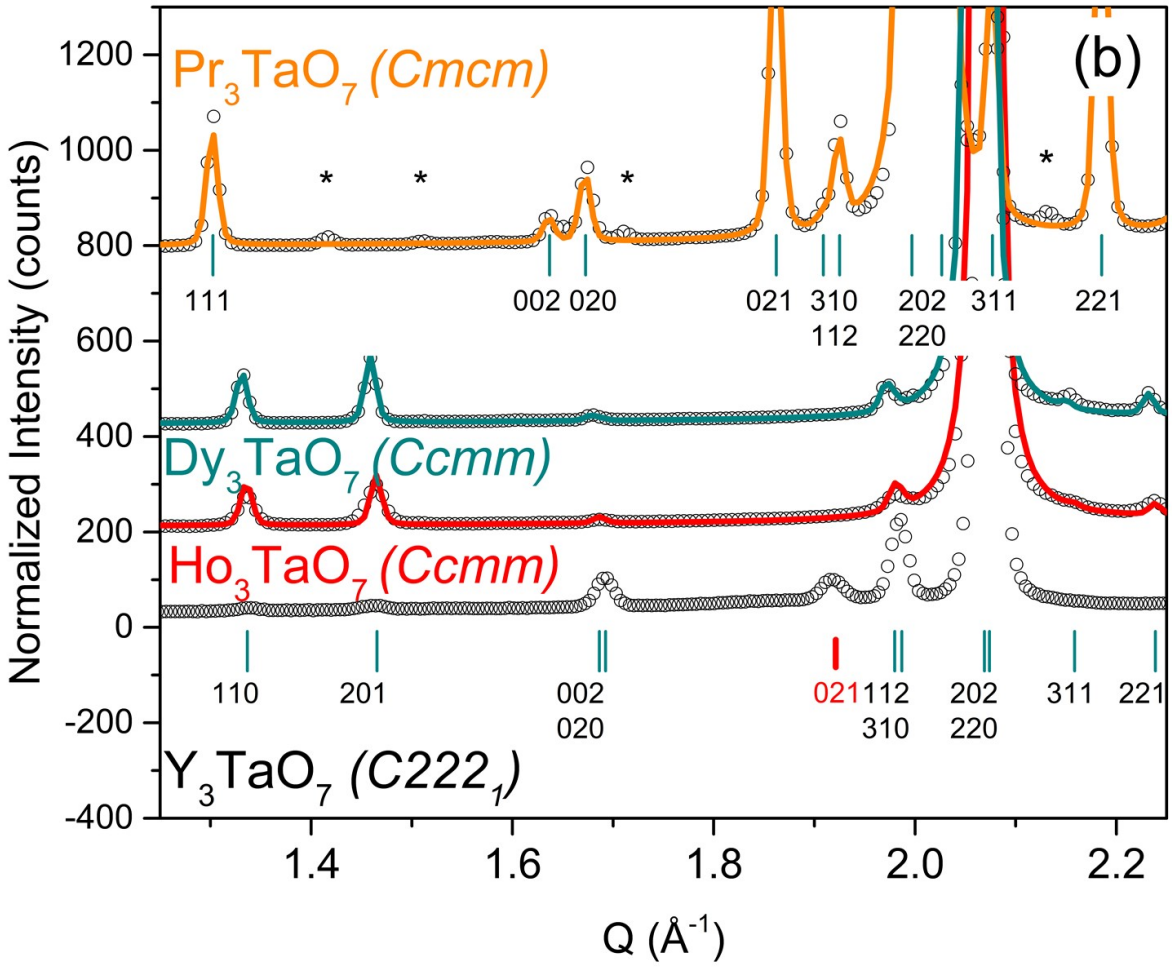

Enlarged version of Figure 2: (a) Stacked high-energy synchrotron X-ray diffraction patterns for A_3TaO_7 (A = Pr, Dy, Ho) as measured (black circles) and modeled (orange, cyan and red curves). Blue curves represent the difference between measurement and calculated model (space groups *Cmcm* and *Ccmm*). The reliability factor (*Rw*) is reported for every sample. Diffraction patterns are offset by values of 10'000 and 20'000 respectively. (b) Expanded view of the low-Q range of (a) using the same color labeling, along with diffraction data of Y_3TaO_7 (black circles), which serves as reference measurement. Cyan ticks represent diffraction conditions allowed in (top) *Cmcm* and (bottom) *Ccmm* space groups. Asterisks (*) mark the $PrTaO_4$ impurity phase reflections for Pr_3TaO_7. The red tick mark at ~1.93 $Å^{-1}$ indicates the location of the (021) diffraction peak, which serves as space group distinction between $C222_1$ and *Ccmm* (and it is only allowed for $C222_1$). Diffraction patterns are offset by values of 200, 400 and 800 respectively. Enlarged version of this figure is available in the supplementary section.

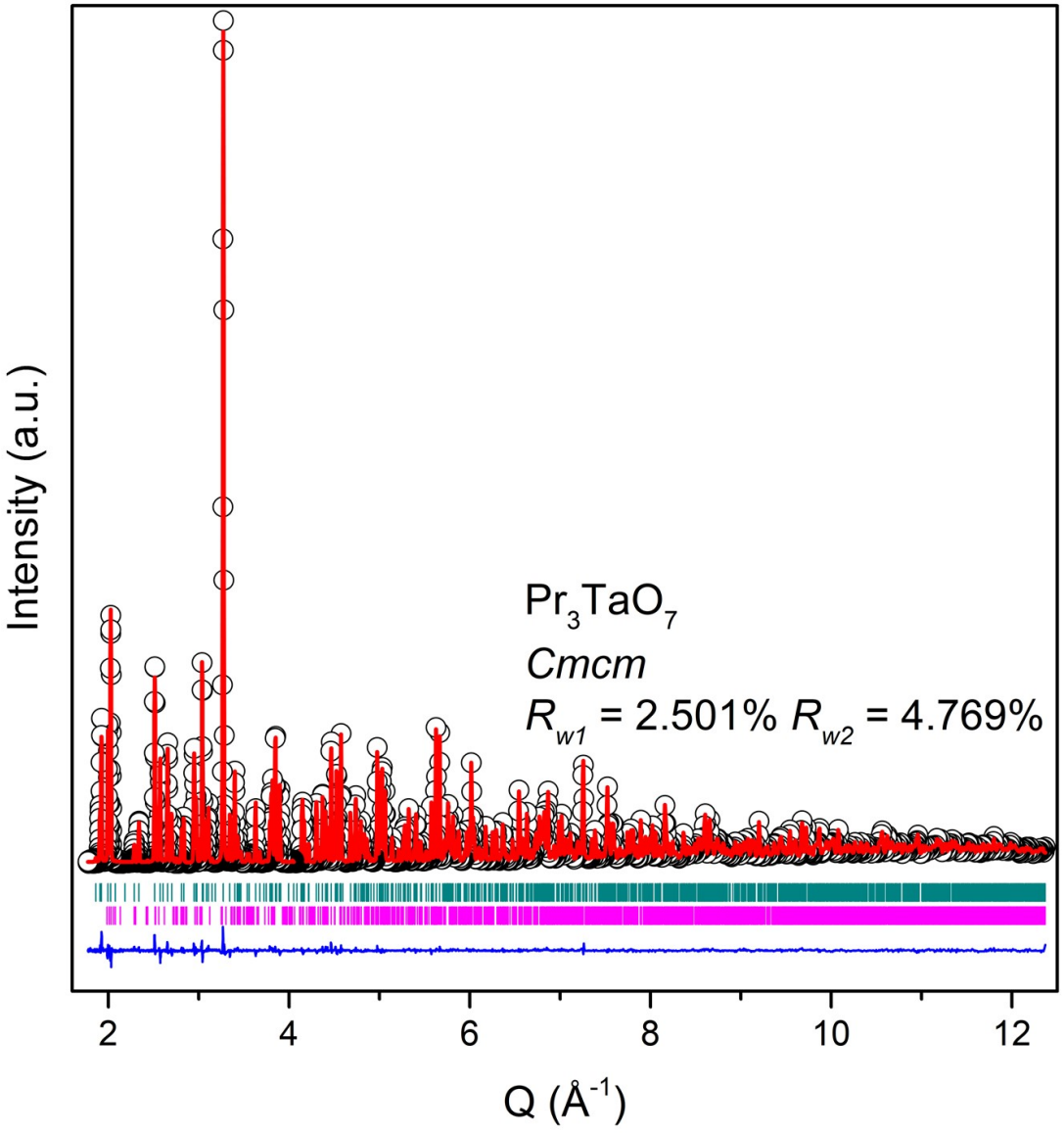

Supplementary Figure 1: POWGEN' high-resolution neutron diffraction pattern of Pr_3TaO_7 measured at room temperature (black circles) and modeled (red curve) using *Cmcm* space group. The blue curve represents the difference curve between measurement and the model fit, with *Rw1* and *Rw2* being the fit reliability factors. Cyan and Magenta ticks indicate the expected Bragg peak positions according to the crystal structure models of Pr_3TaO_7 and $PrTaO_4$ impurity phase respectively.

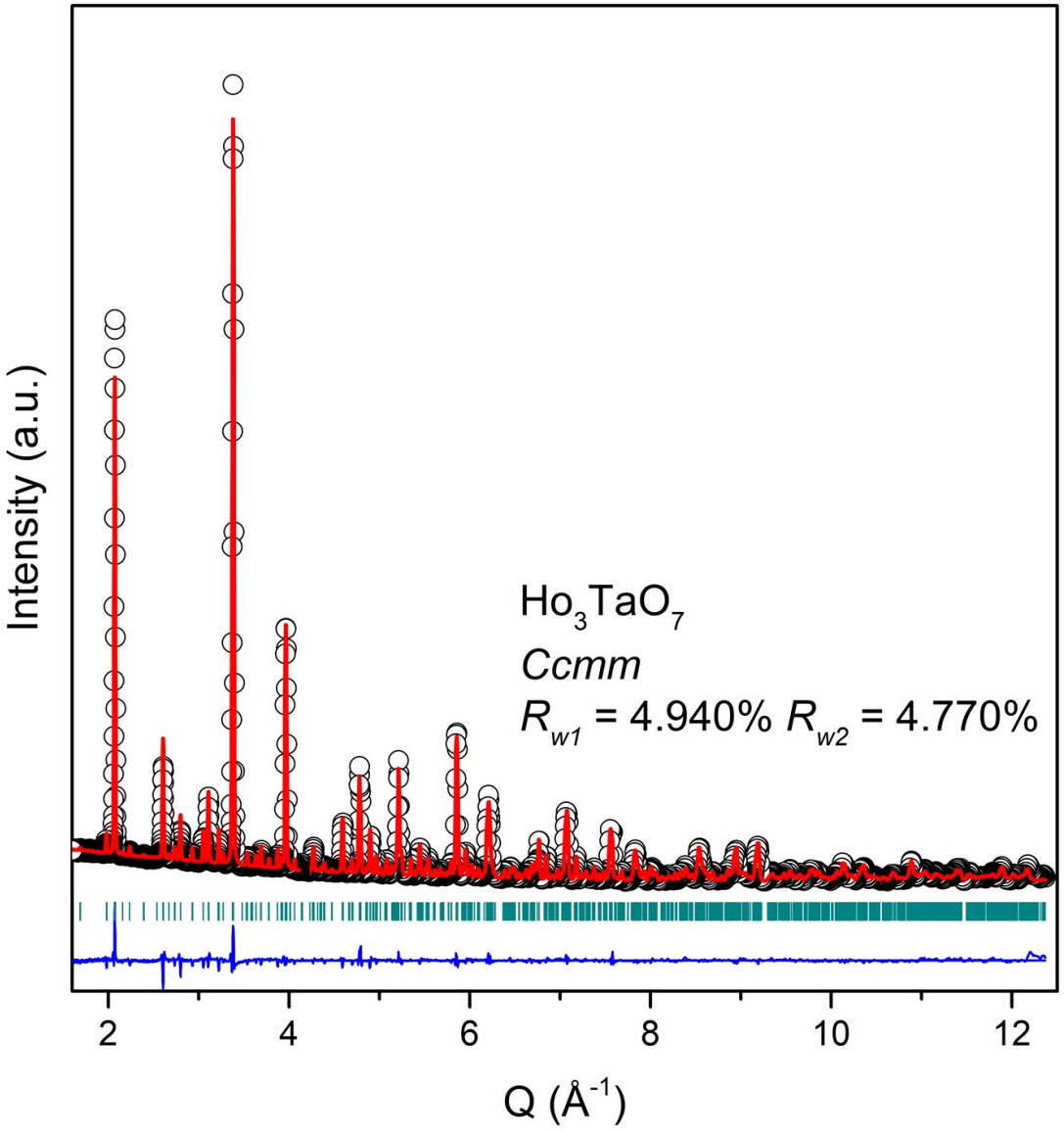

Supplementary Figure 2: POWGEN' high-resolution neutron diffraction pattern of Ho_3TaO_7 measured at room temperature (black circles) and modeled (red curve) using *Ccmm* space group. The blue curve represents the difference curve between measurement and the model fit, with *Rw1* and *Rw2* being the fit reliability factors. Cyan ticks indicate the expected Bragg peak positions according to the crystal structure model.

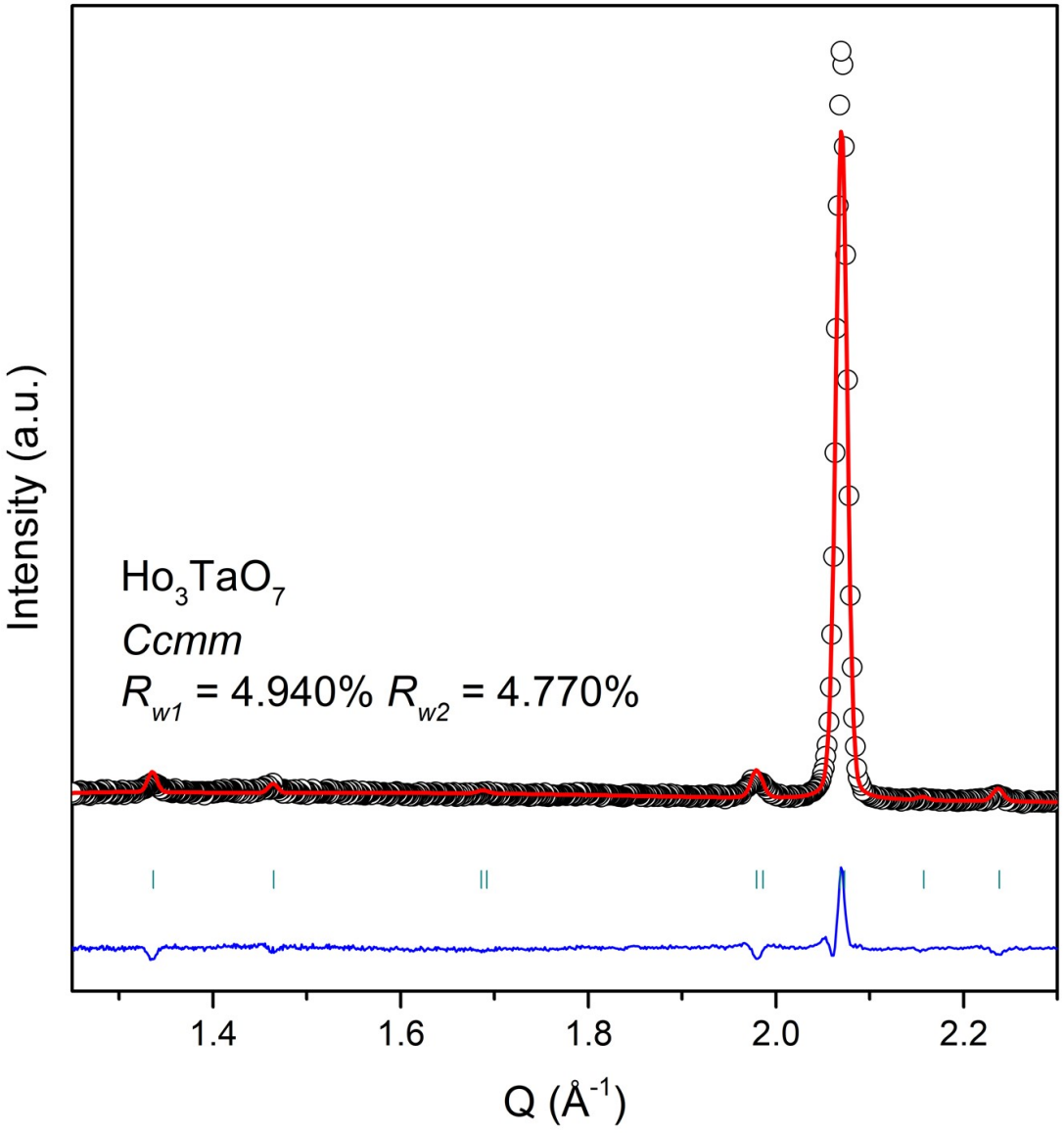

Supplementary Figure 3: An expanded view of low-Q region of POWGEN' high-resolution neutron diffraction pattern of Ho_3TaO_7 measured at room temperature (black circles) and modeled (red curve) using *Ccmm* space group. The blue curve represents the difference curve between measurement and the model fit, with *Rw1* and *Rw2* being the fit reliability factors. Cyan ticks indicate the expected Bragg peak positions according to the crystal structure model.

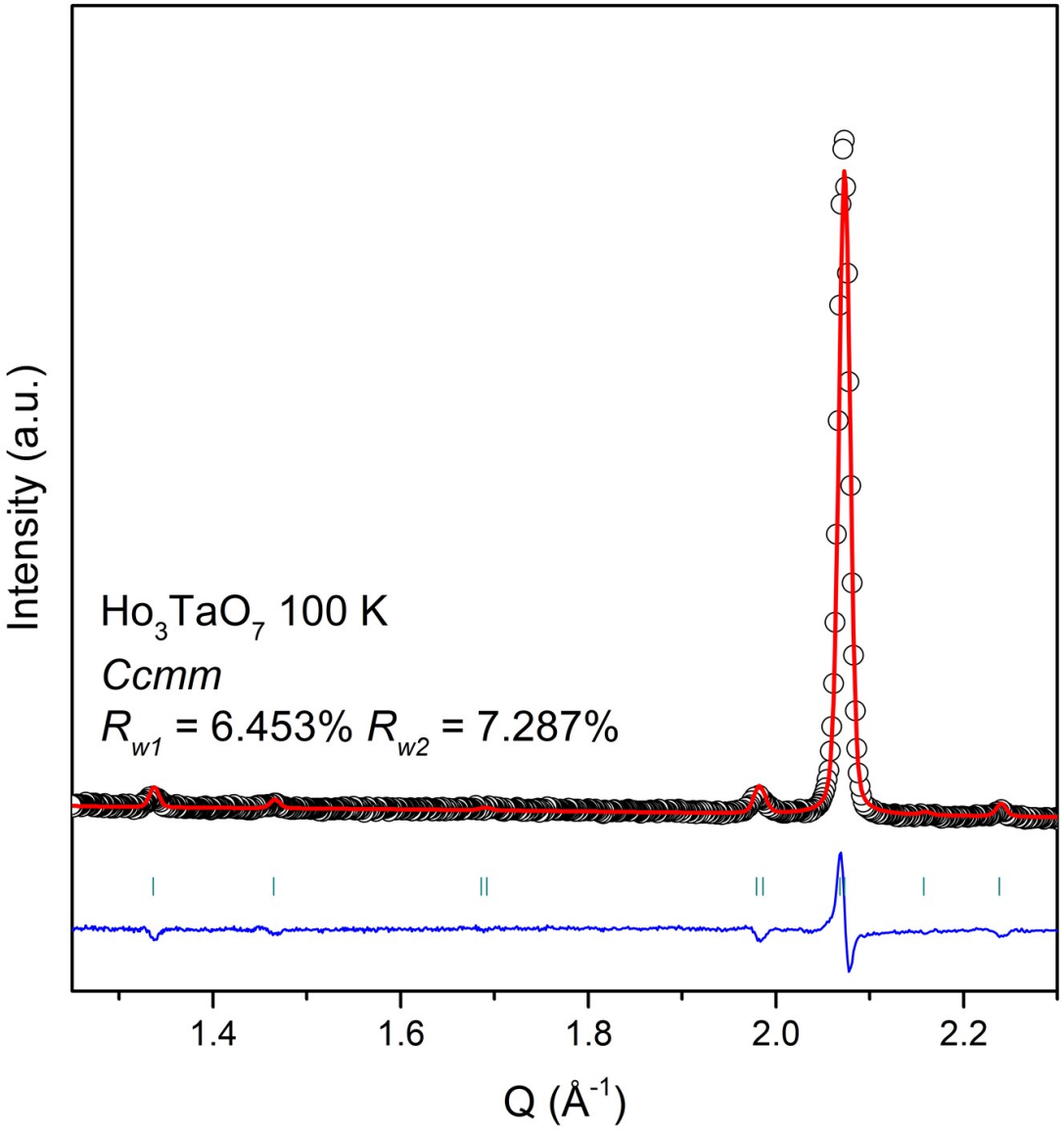

Supplementary Figure 4: Low-Q region of POWGEN' high-resolution neutron diffraction pattern of Ho_3TaO_7 measured at 100 K (black circles) and modeled (red curve) using *Ccmm* space group. The blue curve represents the difference curve between measurement and the model fit, with *Rw1* and *Rw2* being the fit reliability factors. Cyan ticks indicate the expected Bragg peak positions according to the crystal structure model.

Supplementary Table 2: Structural information for long-range diffraction data refinements. Unit cell parameters, fractional positional coordinates and thermal factors are followed by sigma values. NOMAD and POWGEN denote neutron diffraction data collected at respective neutron total scattering instruments while SXRD denotes synchrotron X-ray diffraction data. Uiso denote isotropic thermal factors. When applicable, harmonic thermal factors (Uij) are shown with first row denoting U_{11}, U_{22} and U_{33} factors while U_{12}, U_{13} and U_{23} are shown in the second below.

Pr_3TaO_7 (NOMAD)		**a (Å)**	**b (Å)**	**c (Å)**	
Cmcm (63)		10.98712(17)	7.51112(13)	7.67928(16)	
Atom	**Wyckoff Site**	**x**	**y**	**z**	**Uiso**
Pr1	4b	0	0.5	0	0.0086(5)
Pr2	8g	0.22948(16)	0.7943(3)	0.25	0.0016(3)
Ta1	4a	0	0	0	0.0008(3)
O1	16h	0.37393(11)	0.68544(14)	0.03476(16)	0.0089(3)
O2	8g	0.13001(16)	0.5250(2)	0.25	0.0033(3)
O3	4c	0	0.9332(3)	0.25	0.0073(4)

Tb_3TaO_7 (NOMAD)		**a (Å)**	**b (Å)**	**c (Å)**	
Ccmm (63)		10.5716(2)	7.46997(16)	7.51362(14)	
Atom	**Wyckoff Site**	**x**	**y**	**z**	**Uiso**
Tb1	4b	0.5	0	0	0.0075(3)
Tb2	8g	0.23511(15)	0.2357(2)	0.75	0.0030(2)
Ta1	4a	0	0	0	0.0015(3)
O1	16h	0.37637(16)	0.30011(18)	0.9717(2)	0.0149(4)
O2	4c	0.0614(4)	0	0.75	0.0163(7)
O3	4c	0.6283(3)	0	0.75	0.0018(4)
O4	4c	0.3625(4)	0	0.75	0.0086(6)

Ho_3TaO_7 (NOMAD)		**a (Å)**	**b (Å)**	**c (Å)**	
Ccmm (63)		10.4933(3)	7.4250(2)	7.4553(2)	
Atom	**Wyckoff Site**	**x**	**y**	**z**	**Uiso**
Ho1	4b	0.5	0	0	0.0247(8)
Ho2	8g	0.2404(2)	0.2386(3)	0.75	0.0013(3)
Ta1	4a	0	0	0	0.0171(6)
O1	16h	0.3766(4)	0.2891(4)	0.9745(5)	0.0294(8)
O2	4c	0.0622(7)	0	0.75	0.0227(13)
O3	4c	0.6281(6)	0	0.75	0.0129(9)
O4	4c	0.3621(7)	0	0.75	0.0218(14)

Ho_3TaO_7 (NOMAD)		**a (Å)**	**b (Å)**	**c (Å)**		
Fm-3m (225)		5.25850(11)	5.25850(11)	5.25850(11)		
Atom	**Wyckoff Site**	**x**	**y**	**z**	**Occupancy**	**Uiso**
Ho1	4a	0	0	0	0.75	0.0212(5)
Ta1	4a	0	0	0	0.25	0.0212(5)
O1	8c	0.25	0.25	0.25	0.875	0.0681(8)

Tm_3TaO_7 (NOMAD)		**a (Å)**	**b (Å)**	**c (Å)**		
Fm-3m (225)		5.21362(5)	5.21362(5)	5.21362(5)		
Atom	**Wyckoff Site**	**x**	**y**	**z**	**Occupancy**	**Uiso**
Tm1	4a	0	0	0	0.75	0.0179(3)
Ta1	4a	0	0	0	0.25	0.0179(3)
O1	8c	0.25	0.25	0.25	0.875	0.0595(5)

Yb_3TaO_7 (NOMAD)		**a (Å)**	**b (Å)**	**c (Å)**		
Fm-3m (225)		5.19453(5)	5.19453(5)	5.19453(5)		
Atom	**Wyckoff Site**	**x**	**y**	**z**	**Occupancy**	**Uiso**
Ho1	4a	0	0	0	0.75	0.0214(3)
Ta1	4a	0	0	0	0.25	0.0214(3)
O1	8c	0.25	0.25	0.25	0.875	0.0577(5)

Pr_3TaO_7 (SXRD)		**a (Å)**	**b (Å)**	**c (Å)**	
Cmcm (63)		10.98488(18)	7.51246(12)	7.67712(13)	
Atom	**Wyckoff Site**	**x**	**y**	**z**	**Uiso**
Pr1	4b	0	0.5	0	0.0087(5)
Pr2	8g	0.22797(11)	0.79573(15)	0.25000	0.0031(4)
Ta1	4a	0	0	0	0.0014(4)
O1	16h	0.3740(9)	0.6822(12)	0.0361(12)	0.002(3)
O2	8g	0.1285(16)	0.528(2)	0.25	0.012(4)
O3	4c	0	0.9421(27)	0.25	0.003(6)

Dy_3TaO_7 (SXRD)		**a (Å)**	**b (Å)**	**c (Å)**	
Ccmm (63)		10.52150(19)	7.43849(13)	7.48792(10)	
Atom	**Wyckoff Site**	**x**	**y**	**z**	**Uiso**
Dy1	4b	0.5	0	0	0.0109(6)
Dy2	8g	0.23408(9)	0.23493(13)	0.75	0.0069(3)
Ta1	4a	0	0	0	0.0044(5)
O1	16h	0.3778(12)	0.3046(15)	0.9685(13)	0.002(3)
O2	4c	0.058(3)	0	0.75	0.018(7)
O3	4c	0.630(3)	0	0.75	0.003(6)
O4	4c	0.357(3)	0	0.75	0.009(7)

Ho_3TaO_7 (SXRD)		**a (Å)**	**b (Å)**	**c (Å)**	
Ccmm (63)		10.4852(3)	7.4241(2)	7.45141(17)	
Atom	**Wyckoff Site**	**x**	**y**	**z**	**Uiso**
Ho1	4b	0.5	0	0	0.0131(9)
Ho2	8g	0.23721(14)	0.23741(19)	0.75	0.0111(4)
Ta1	4a	0	0	0	0.0074(8)
O1	16h	0.377(2)	0.298(3)	0.971(2)	0.007(6)
O2	4c	0.060(4)	0	0.75	0.018(11)
O3	4c	0.631(5)	0	0.75	0.027(13)
O4	4c	0.358(5)	0	0.75	0.026(14)

Pr_3TaO_7 (POWGEN, RT)	**a (Å)**	**b (Å)**	**c (Å)**			
Cmcm (63)	10.98883(4)	7.51223(3)	7.68015(3)			
Atom	**Wyckoff Site**	**x**	**y**	**z**	$\frac{U_{11}}{U_{12}}$	$\frac{U_{22}}{U_{13}}$	$\frac{U_{33}}{U_{23}}$
Pr1	4b	0	0.5	0	0.0062(5) 0	0.0249(8) 0	0.0027(5) -0.0022(10)
Pr2	8g	0.22838(8)	0.79583(12)	0.25	0.0056(4) -0.0007(6)	0.0083(5) 0	0.0037(3) 0
Ta1	4a	0	0	0	0.0017(3) 0	0.0062(4) 0	0.0009(3) 0.0000(5)
O1	16h	0.37429(5)	0.68615(9)	0.03461(7)	0.0116(3) 0.0126(5)	0.0239(3) -0.0009(4)	0.0056(2) -0.0035(4)
O2	8g	0.13092(7)	0.52372(11)	0.25	0.0053(3) -0.0003(6)	0.0086(4) 0	0.0065(3) 0
O3	4c	0	0.93200(15)	0.25	0.0125(5) 0	0.0110(5) 0	0.0006(4) 0

Ho_3TaO_7 (POWGEN, RT)	**a (Å)**	**b (Å)**	**c (Å)**			
Ccmm (63)	10.48914(18)	7.42688(14)	7.45209(13)			
Atom	**Wyckoff Site**	**x**	**y**	**z**	$\frac{U_{11}}{U_{12}}$	$\frac{U_{22}}{U_{13}}$	$\frac{U_{33}}{U_{23}}$
Ho1	4b	0.5	0	0	0.0055(13) 0	0.0122(14) -0.0031(17)	0.0077(12) 0
Ho2	8g	0.23578(15)	0.2354(2)	0.75	0.0053(7) 0.0016(11)	0.0036(7) 0	0.0039(8) 0
Ta1	4a	0	0	0	0.0006(12) 0	0.0031(13) 0.0032(18)	0.0026(11) 0
O1	16h	0.3761(2)	0.2999(3)	0.9711 (3)	0.0116(9) -0.0057(15)	0.0191(9) 0.0035(15)	0.0171(10) -0.0063(13)
O2	4c	0.0675(4)	0	0.75	0.0180(18) 0	0.0106(19) 0	0.0058(16) 0
O3	4c	0.6306(4)	0	0.75	0.0015(15) 0	0.0033(14) 0	0.0069(15) 0
O4	4c	0.3620(4)	0	0.75	0.0047(17) 0	0.0089(17) 0	0.0111(16) 0

Supplementary Table 3: Structural information for room temperature (RT) short-range PDF data refinements. Unit cell parameters, fractional positional coordinates and thermal factors are followed by sigma values.

Pr_3TaO_7 (PDF, RT)		**a (Å)**	**b (Å)**	**c (Å)**			
Cmcm (63)		10.995(4)	7.523(3)	7.6858(18)			
Atom	**Wyckoff Site**	**x**	**y**	**z**	$\frac{U_{11}}{U_{12}}$	$\frac{U_{22}}{U_{13}}$	$\frac{U_{33}}{U_{23}}$
Pr1	4b	0	0.5	0	0.0094(18) 0	0.044(4) 0	0.001(1) -0.003(2)
Pr2	8g	0.2290(3)	0.2041(5)	0.25	0.0061(9) -0.0018(6)	0.008(1) 0	0.0072(9) 0
Ta1	4a	0	0	0	0.0019(6) 0	0.0071(11) 0	0.0055(8) -0.0005(6)
O1	16h	0.37592(18)	0.3116(4)	0.0367(3)	0.0119(9) -0.013(1)	0.0279(17) -0.0025(5)	0.0066(5) 0.0043(7)
O2	8g	0.1306(3)	0.4767(5)	0.25	0.0074(8) 0.0004(8)	0.0061(8) 0	0.0080(7) 0
O3	4c	0	0.0646(5)	0.25	0.0157(14) 0	0.003(1) 0	0.0042(7) 0

Tb_3TaO_7 (PDF, RT)		**a (Å)**	**b (Å)**	**c (Å)**			
Ccmm (63)		10.529(6)	7.492(3)	7.514(3)			
Atom	**Wyckoff Site**	**x**	**y**	**z**	$\frac{U_{11}}{U_{12}}$	$\frac{U_{22}}{U_{13}}$	$\frac{U_{33}}{U_{23}}$
Tb1	4b	0.5	0	0	0.0073(19) 0	0.049(4) 0.0068(9)	0.0083(14) 0
Tb2	8g	0.2324(2)	0.2378(5)	0.75	0.0086(6) 0.0022(5)	0.0045(6) 0	0.0094(7) 0
Ta1	4a	0	0	0	0.0152(19) 0	0.005(1) 0.0044(11)	0.0108(15) 0
O1	16h	0.3766(3)	0.3029(5)	0.9680(5)	0.0178(12) -0.020(1)	0.0358(15) 0.0067(7)	0.0108(8) -0.0072(9)
O2	4c	0.0641(6)	0	0.75	0.0132(18) 0	0.0066(14) 0	0.0102(15) 0
O3	4c	0.6308(5)	0	0.75	0.0020(9) 0	0.0120(14) 0	0.0107(16) 0
O4	4c	0.3641(5)	0	0.75	0.0071(11) 0	0.0081(13) 0	0.0028(9) 0

Ho_3TaO_7 (PDF, RT)		**a (Å)**	**b (Å)**	**c (Å)**			
Ccmm (63)		10.458(7)	7.440(4)	7.457(4)			
Atom	**Wyckoff Site**	**x**	**y**	**z**	$\frac{U_{11}}{U_{12}}$	$\frac{U_{22}}{U_{13}}$	$\frac{U_{33}}{U_{23}}$
Ho1	4b	0.5	0	0	0.0056(17) 0	0.083(7) -0.0054(14)	0.0045(12) 0
Ho2	8g	0.2313(4)	0.2412(6)	0.75	0.0109(9) 0.0030(8)	0.0041(6) 0	0.01476(13) 0
Ta1	4a	0	0	0	0.014(2) 0	0.0054(16) 0.0065(15)	0.010(3) 0
O1	16h	0.3778(3)	0.2965(7)	0.9709(8)	0.0139(14) -0.0158(14)	0.028(2) 0.0015(13)	0.0137(13) 0.0002(18)
O2	4c	0.0619(9)	0	0.75	0.017(3) 0	0.009(3) 0	0.009(3) 0
O3	4c	0.6276(9)	0	0.75	0.009(3) 0	0.0078(15) 0	0.011(3) 0

O4	4c	0.3624(8)	0	0.75	0.002(1) 0	0.012(3) 0	0.0077(19) 0

Ho_3TaO_7 (PDF) *Fm-3m* (225)		**a (Å)** 5.2708(6)	**b (Å)** 5.2708(6)	**c (Å)** 5.2708(6)		
Atom	**Wyckoff Site**	**x**	**y**	**z**	**Occupancy**	**Uiso**
Ho1	4a	0	0	0	0.75	0.0201(3)
Ta1	4a	0	0	0	0.25	0.0201(3)
O1	8c	0.25	0.25	0.25	0.875	0.0590(5)

Tm_3TaO_7 (PDF) *Fm-3m* (225)		**a (Å)** 5.2267(5)	**b (Å)** 5.2267(5)	**c (Å)** 5.2267(5)		
Atom	**Wyckoff Site**	**x**	**y**	**z**	**Occupancy**	**Uiso**
Tm1	4a	0	0	0	0.75	0.0215(3)
Ta1	4a	0	0	0	0.25	0.0215(3)
O1	8c	0.25	0.25	0.25	0.875	0.0627(5)

Yb_3TaO_7 (PDF) *Fm-3m* (225)		**a (Å)** 5.2093(3)	**b (Å)** 5.2093(3)	**c (Å)** 5.2093(3)		
Atom	**Wyckoff Site**	**x**	**y**	**z**	**Occupancy**	**Uiso**
Yb1	4a	0	0	0	0.75	0.0234(3)
Ta1	4a	0	0	0	0.25	0.0234(3)
O1	8c	0.25	0.25	0.25	0.875	0.0623(3)

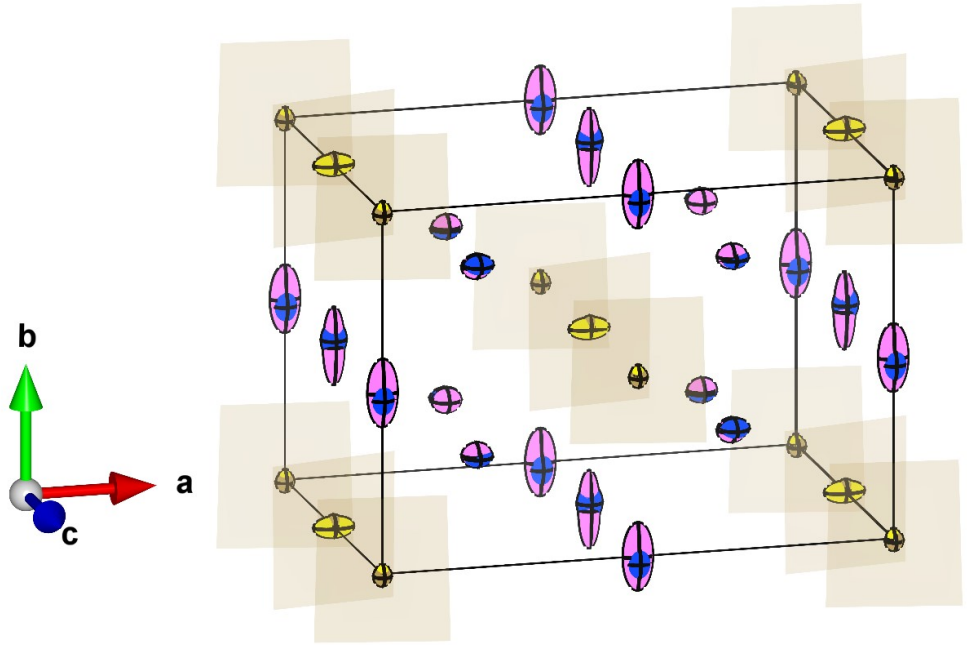

Supplementary Figure 5: Overlayed $C222_1$ (Γ_1-) and C2/m (Γ_3+) Ho_3TaO_7 structural models from short-range PDF refinement performed at 100 K. Solid black lines indicate the respective unit cell while shaded brown regions represent TaO_6 octahedra. Ta and Ho cations in respective atomic sites in the $C222_1$ structure are indicated as solid dark brown and blue ellipsoids, while Ta and Ho cations in respective atomic sites in the C2/m structure are indicated as solid yellow and pink ellipsoids. The ellipsoids represent the extent of anisotropic thermal vibrations, U_{11}, U_{22} and U_{33}.

Supplementary Table 4: Structural information for localized 100 K temperature short-range PDF data refinements. Unit cell parameters, fractional positional coordinates and thermal factors are followed by sigma values.

Pr_3TaO_7 (PDF, 100K)		**a (Å)**	**b (Å)**	**c (Å)**	
C2cm (40)		10.988(4)	7.490(3)	7.681(3)	
Atom	**Wyckoff Site**	**x**	**y**	**z**	**Uiso**
Pr1	4a	0.5042(14)	0	0	0.0109(9)
Pr2	4b	0.2300(7)	0.2015(11)	0.25	0.0042(8)
Pr3	4b	0.2758(7)	0.705(1)	0.25	0.0034(6)
Ta1	4a	0.0054(7)	0	0	0.0047(3)
O1	8c	0.8709(5)	0.8254(7)	0.037(1)	0.0090(6)
O2	8c	0.625	0.3059(6)	0.4632(8)	0.0053(4)
O3	4b	0.1337(7)	0.4686(9)	0.25	0.0057(6)
O4	4b	0.3751(6)	0.9833(8)	0.25	0.0046(6)
O5	4b	0.9982(8)	0.0716(6)	0.25	0.0049(5)

Ho_3TaO_7 (PDF, 100K)		**a (Å)**	**b (Å)**	**c (Å)**	
$C222_1$ (20)		10.486(5)	7.419(3)	7.445(2)	
Atom	**Wyckoff Site**	**x**	**y**	**z**	**Uiso**
Ho1	4a	0	0.4810(7)	0	0.0080(5)
Ho2	8c	0.2349(3)	0.2362(4)	0.7451(7)	0.0062(3)
Ta1	4a	0	0.9960(7)		0.0029(4)
O1	8c	0.3726(5)	0.3122(7)	0.9639(8)	0.0098(7)
O2	8c	0.3775(4)	0.2899(5)	0.5230(7)	0.0060(6)
O3	4b	0.0667(5)	0	0.75	0.0073(5)
O4	4b	0.6281(8)	0	0.75	0.0076(5)
O5	4b	0.3628(7)	0	0.75	0.0084(8)

Ybr_3TaO_7 (PDF, 100K)		**a (Å)**	**b (Å)**	**c (Å)**	
C2mm (38)		10.558(4)	7.171(3)	7.443(3)	
Atom	**Wyckoff Site**	**x**	**y**	**z**	**Uiso**
Yb1	4c	0.4799(5)	0	0.7210(4)	0.0104(4)
Yb2	4d	0.2166(5)	0.7499(8)	0	0.0124(5)
Yb3	4e	0.2289(5)	0.2508(6)	0.5	0.0077(5)
Ta1	4c	0.9996(6)	0	0.7328(6)	0.0037(4)
O1	8f	0.5929(6)	0.2684(4)	0.2656(5)	0.0072(5)
O2	8f	0.875000	0.7589(8)	0.1839(5)	0.0116(6)
O3	2a	0.0379(11)	0	0	0.012(2)
O4	2b	0.9520(8)	0	0.5	0.007(1)
O5	2a	0.6156(13)	0	0	0.019(1)
O6	2b	0.3598(13)	0	0.5	0.019(1)
O7	2a	0.3755(18)	0	0	0.019(1)
O8	2b	0.6089(16)	0	0.5	0.019(1)